The Astrophysical Journal Supplement Series, 262:22 (22pp), 2022 September https://doi.org/10.3847/1538-4365/ac7be6

Simulating the Legacy Survey of Space and Time Stellar Content with TRILEGAL

Piero Dal Tio[1,2], Giada Pastorelli[3], Alessandro Mazzi[1,2], Michele Trabucchi[4], Guglielmo Costa[1], Alice Jacques[5], Adriano Pieres[6,7], Léo Girardi[2], Yang Chen[8,9], Knut A. G. Olsen[5], Mario Juric[10], Željko Ivezić[10], Peter Yoachim[10], William I. Clarkson[11], Paola Marigo[1], Thaise S. Rodrigues[2], Simone Zaggia[2], Mauro Barbieri[12], Yazan Momany[2], Alessandro Bressan[13], Robert Nikutta[5], and Luiz Nicolaci da Costa[6,7]
[1] Dipartimento di Fisica e Astronomia Galileo Galilei, Università di Padova, Vicolo dell'Osservatorio 3, I-35122 Padova, Italy
[2] Osservatorio Astronomico di Padova—INAF, Vicolo dell'Osservatorio 5, I-35122 Padova, Italy; leo.girardi@oapd.inaf.it
[3] Space Telescope Science Institute, 3700 San Martin Drive, Baltimore, MD 21218, USA
[4] Department of Astronomy, University of Geneva, Ch. Pegasi 51, CH-1290 Versoix, Switzerland
[5] NSF's National Optical-Infrared Astronomy Research Laboratory, 950 N. Cherry Ave., Tucson, AZ 85719, USA
[6] Laboratório Interinstitucional de e-Astronomia—LIneA, Rua Gal. José Cristino 77, Rio de Janeiro, RJ—20921-400, Brazil
[7] Observatório Nacional, Rua Gal. José Cristino 77, Rio de Janeiro, RJ—20921-400, Brazil
[8] Anhui University, Hefei 230601, People's Republic of China
[9] National Astronomical Observatories, Chinese Academy of Sciences, Being 100101, People's Republic of China
[10] DiRAC Institute and the Department of Astronomy, University of Washington, Seattle, WA, USA
[11] Department of Natural Sciences, University of Michigan-Dearborn, 4901 Evergreen Road, Dearborn, MI 48128, USA
[12] Universidad de Atacama, Instituto de Astronomia y Ciencias Planetarias, Copiapó, Chile
[13] SISSA, via Bonomea 365, I-34136 Trieste, Italy
Received 2022 April 5; revised 2022 June 22; accepted 2022 June 22; published 2022 August 26

Abstract

We describe a large simulation of the stars to be observed by the Vera C. Rubin Observatory Legacy Survey of Space and Time (LSST). The simulation is based on the TRILEGAL code, which resorts to large databases of stellar evolutionary tracks, synthetic spectra, and pulsation models, added to simple prescriptions for the stellar density and star formation histories of the main structures of the Galaxy, to generate mock stellar samples through a population synthesis approach. The main bodies of the Magellanic Clouds are also included. A complete simulation is provided for single stars, down to the $r = 27.5$ mag depth of the coadded Wide–Fast–Deep survey images. A second simulation is provided for a fraction of the binaries, including the interacting ones, as derived with the BinaPSE module of TRILEGAL. We illustrate the main properties and numbers derived from these simulations, including: comparisons with real star counts; the expected numbers of Cepheids, long-period variables, and eclipsing binaries; the crowding limits as a function of seeing and filter; the star-to-galaxy ratios. Complete catalogs are accessible through the NOIRLab Astro Data Lab, while the stellar density maps are incorporated in the LSST metrics analysis framework.

Unified Astronomy Thesaurus concepts: Large Magellanic Cloud (903); Small Magellanic Cloud (1468); Local Group (929); Galactic bulge (2041); Milky Way Galaxy (1054)

1. Introduction

The Vera C. Rubin Observatory Legacy Survey of Space and Time (LSST; LSST Science Collaboration et al. 2009), with its approach of performing a single survey to tackle a wide variety of science goals, will promote a new era of discovery in astrophysics. Its Wide–Fast–Deep (WFD) main survey will reach unprecedented photometric depths across huge areas of the sky, in six optical filters. Its time-series photometry, being performed along 10 yr with several hundred pointings per field, is likely to reveal stellar variability in ranges of period and amplitude that present-day surveys just barely cover. We refer the reader to Ivezić et al. (2019) for the design of the Rubin Observatory as informed by its main scientific objectives, and to Bianco et al. (2022) for a comprehensive presentation of the Rubin observatory and its efforts to optimize its science return using input from the community.

The definition of LSST passes through a long process in which the scientific performance is simulated under different assumptions about the footprint and the sequence of visits in all filters (Jones et al. 2014; Bianco et al. 2022), as detailed in the several articles of this Focus Issue. Our paper addresses the issue of supporting this process by means of a realistic stellar catalog for any location in the Milky Way galaxy, which is obviously crucial for nearly all science that will be performed by Rubin—as the Milky Way will be an unavoidable component of the source population for any Rubin Observatory pointing. As a consequence of the LSST unprecedented depths, cadences, and coverage of the sky, we cannot simply recur to current stellar catalogs for this aim. One has rather to resource to simulations that, starting from the stars that we already see in present surveys, give a reasonable guess of the stars that will be seen in new, unexplored ranges of brightness and cadence.

Until recently, simulations of the LSST stellar content were based on the galfast code (Jurić 2018). galfast is a classical "Galactic star counts model" that describes the photometry of stars distributed across the main Milky Way components (thin and thick disks, bulge, halo) and their extinction by interstellar dust. The model parameters are calibrated by fitting star counts from the Sloan Digital Sky Survey over 8000 deg^2 of the sky (see Ivezić et al. 2008; Jurić et al. 2008; Bond et al. 2010). A main characteristic of

galfast is its speed, which allows the generation of realistic catalogs to full LSST depth in just a few hours.

In this paper, we describe a new simulation of the LSST stellar content, based on a recent version of the TRIdimensional modeL of thE GALaxy (TRILEGAL) code (Girardi et al. 2005, 2012; Marigo et al. 2017). Although TRILEGAL works based on principles very similar to galfast, it includes a wider variety of the physical and population effects expected to be probed by LSST observations. Moreover, TRILEGAL is still under active development, providing a suitable platform to include new kinds of stars (e.g., asymptotic giant branch stars and white dwarfs of different spectral/chemical types, fast rotators) and time-dependent phenomena (e.g., stellar pulsation, binary eclipses) in the simulations. On the other hand, TRILEGAL is calibrated using different photometric data; therefore it provides an alternative—hence a minimum uncertainty—to the star counts predicted by galfast. Another distinct characteristic of TRILEGAL is the presence of the new module BinaPSE (Dal Tio et al. 2021), recently developed to describe populations of binaries, including interacting ones. All these characteristics make TRILEGAL significantly slower than galfast—but anyway suitable to produce a few improved simulations before LSST operations start.

In this paper, we describe one of such simulations, built both to assist the work of the Survey Cadence Optimization Committee (SCOC), and as a first attempt to simulate a wider variety of stellar phenomena than previously available. The simulation is included in the LSST Metrics Analysis Framework (MAF; Jones et al. 2014), the software package extensively used to evaluate the metrics related to a wide variety of science goals and possible survey configurations (see Bianco et al. 2022 for more details). Our codes, input data and methods are described in Section 2. The derived databases are presented in Section 3, and their properties are illustrated in Section 4. Ongoing efforts to improve the simulations are briefly mentioned in Section 5.

2. Input Data and Methods

2.1. General Strategy, Footprint, and Filters

Our goal is to simulate all stars visible on the final stacked LSST images, across the entire sky possibly covered by the LSST main survey. The first requirement implies reaching the coadded survey depth of $r < 27.5$ mag (Ivezić et al. 2008). At the time this project started, the second requirement translated in a sky footprint made by the intersection of all areas with

1. decl. $\delta < 5°$;
2. ecliptic latitude $\beta < 10°$;
3. within $|b| < 10°$ of the Galactic plane and with $\delta < 35°$.

This choice does not reflect the latest recommendations by the SCOC (from August 2021) to extend the WFD coverage up to $\delta < 12°$, at least in areas not strongly affected by extinction. Essentially, this means that present simulations are incomplete in a strip of the sky of decl. $5° < \delta < 12°$ and spanning the interval $12\,\mathrm{hr} \lesssim \alpha \lesssim 18.5\,\mathrm{hr}$.

The simulations of this footprint are performed twice: first including just single stars with the classical TRILEGAL code, then including just the binaries using the BinaPSE module of TRILEGAL. The two distinct output files can then be mixed by assuming a given initial binary fraction (see Section 3.2 below).

Table 1
Evolutionary Phases of Individual Stars

label	Evolutionary Phase
0	Pre-main sequence (single stars; PMS)
1	Main sequence (MS)
2	Hertzsprung gap
3	Red giant branch (RGB)
4–6	Core helium burning (CHeB)
7	Early asymptotic giant branch (EAGB)
8	Thermally pulsing AGB (TPAGB)
9	Post-AGB
10	CO-WD
21	Helium main sequence
22	Helium Hertzsprung gap
23	Helium giant branch
24	He-WD
25	ONe-WD
26	Neutron star
27	Black hole

Note. Labels > 20 refer to the products of binary evolution.

Simulated stars include the photometry in all LSST u, g, r, i, z, y AB magnitudes, plus the Gaia G, $G_{\rm BP}$, $G_{\rm RP}$ Vega magnitudes. More specifically, stars simulated in the luminosity-effective temperature–metallicity space are converted into the LSST+Gaia photometry using bolometric correction tables and extinction coefficients computed with the YBC code by Chen et al. (2019). For LSST we adopt the total throughputs provided in Docushare Collection 1777 (2012 March), resulting from the combination of mirrors, lenses, filter, detector, and the atmosphere at an airmass of 1.2. Filter throughtputs for Gaia come from Maíz Apellániz & Weiler (2018). Extinction coefficients are derived in a consistent way from the O'Donnell (1994) extinction curve with $R_V = 3.1$.

TRILEGAL output includes, in addition to several intrinsic stellar properties (photometry, surface composition and gravity, expected pulsation periods, etc.), a few positional and kinematic properties, such as the distances, proper motions, and space velocities. The latter are computed in a very approximate way, just extrapolating for all stars in each galactic component the properties of velocities ellipsoids measured in the solar vicinity (Dehnen & Binney 1998; Chiba & Beers 2000; Dias & Lépine 2005; Holmberg et al. 2009) while assuming cylindrical symmetry, or, in the case of the bulge, the same kinematics as in Robin et al. (2003). These approximations therefore do not follow the Jeans equation and the expected changes of kinematics across the MW. Nonetheless, such space velocities are still very useful to check the expected changes in kinematic properties across the color–magnitude diagram (CMD), especially for stars within moderate distances from the Sun (up to a few kiloparsecs), as illustrated in Rossetto et al. (2011).

2.2. Single Stars in the MW

To simulate single stars, we use the same evolutionary tracks as in Marigo et al. (2017), namely, PARSEC v1.2S (Bressan et al. 2012) plus COLIBRI PR16 (Marigo et al. 2013; Rosenfield et al. 2016). They are complemented with post-AGB tracks from Miller Bertolami (2016) and WD cooling tracks from Renedo et al. (2010). Table 1 describes all the

evolutionary phases present in the tracks, as labeled inside the TRILEGAL code and on its output.

These tracks, once converted into isochrones, provide the HR position of stars of given age, metallicity, and initial mass. In addition, TRILEGAL also keeps track of many other stellar properties, such as the current mass, mass-loss rate, and surface chemical composition. These quantities are tabulated and used to derive pulsation properties of classical Cepheids and long-period variables (as detailed in Sections 4.4 and 4.5 below).

Stars are spatially distributed according to a stellar density profile that comprehends four distinct Galaxy components—thin and thick disks, halo and bulge—each one with its own star formation and chemical enrichment history. Details about these components, and their calibration using photometric data from several sources, can be found in Girardi et al. (2005, 2012), and more recently in Table 1 of Pieres et al. (2020) and Table 1 of Mazzi et al. (2021). These functions specify the likelihood of simulating stars as a function of the spatial coordinates, age, and metallicity. In addition, the likelihood of having stars with different initial masses is specified by the initial mass function (IMF) from Chabrier (2001). It is important to note that the functions and parameters we use to describe the thin disk and bulge are those mentioned in both Pieres et al. (2020) and Mazzi et al. (2021), while for the thick disk and halo we use those mentioned in Mazzi et al. (2021): essentially, we use a squared hyperbolic secant with scale height of 800 pc for the thick disk, and an oblate power-law with exponent 2.75 and oblateness 0.62 for the halo. Nonetheless, the most updated description of the thick disk and halo using TRILEGAL is nowadays the one from Pieres et al. (2020), which was still ongoing work when our LSST simulations started.

Every run of TRILEGAL represents a conic section of the MW, characterized by its central coordinates, total area, extinction at infinity, and the rms variation of this extinction across the area. The latter two numbers are derived from extinction-at-infinity maps. The total extinction at infinity is distributed along the line of sight, as if it were produced inside an exponential layer of dust with a scale height of 110 pc.

To obtain the total extinction at infinity, we adopt the Planck Collaboration et al. (2014) dust maps provided using the Hierarchical Equal Area isoLatitude Pixelization (HEALPix; Górski et al. 2005) with a resolution of $5'$ ($n_{\rm side} = 2048$). More specifically we follow the recommendations from the Planck Collaboration and adopt $E(B-V) = E(B-V)_{\rm xgal}$ if $E(B-V)_{\rm xgal} < 0.3$ mag, and $E(B-V) = 1.49 \times 10^4 \tau_{353}$ otherwise. These maps are then converted into $A_V = 3.1\, E(B-V)$ and reduced to the resolution of our simulations. Each HEALPix is then characterized by its mean A_V—illustrated in the top panel of Figure 1—and its standard deviation.

That said, to perform our simulations we could split the LSST footprint into many equal-area fields, e.g., by adopting the healpixels of any $n_{\rm side} \leqslant 2048$. However, favoring much smaller values of $n_{\rm side}$ leads to a significant reduction in the total computing time—but also to inaccurate results where the extinction or the predicted stellar number density vary significantly within a given field. Therefore, we perform large-area simulations by adopting a variable resolution. Starting from an initial resolution of $n_{\rm side} = 64$, any pixel that does not satisfy specific constraints on "surface mass density" and extinction variations is split into four smaller pixels. The procedure is repeated until the maximum resolution defined by $n_{\rm side} = 1024$ is reached. We impose $\sigma_{A_V} \leqslant \min(0.1A_V, 3.0)$ and $\sigma_{\rm SD} \leqslant 5\%$ as tolerance on extinction and surface mass density variations within each pixel. The surface mass density is defined as the projected mass of the Galaxy components per square degree (bottom panel of Figure 1), as predicted using the Girardi et al. (2012) calibration of TRILEGAL.

2.3. Binaries in the MW

The classical TRILEGAL code does not allow the simulation of close and interacting binaries, which are expected to be among the most interesting objects in the multiwavelength, multiepoch photometry of LSST. This motivated us to expand TRILEGAL capabilities by linking it with the BSE code (Hurley et al. 2002), a popular binary evolution code for population synthesis. We revised BSE to transform it into a grid-based code in order to satisfy our accuracy requirements and to make future changes of evolutionary grids much easier. The BSE revision led to the creation of a new TRILEGAL module named BinaPSE (Dal Tio et al. 2021). It shares with TRILEGAL the evolutionary grids and interpolation routines but preserves the binary evolution methodology described in Hurley et al. (2002). Table 2 lists all stellar kinds present in BinaPSE and BSE.

For the probability distribution of mass ratios and initial orbital parameters we adopt the prescriptions suggested by Eggleton (2006). A random orientation has been subsequently attributed to the orbits of binary systems in order to simulate their radial velocity and light curves, as well as the occurrence of eclipses. Several aspects of this procedure are illustrated in the study of the Gaia sample within a 200 pc distance by Dal Tio et al. (2021).

The simulations of binaries on the LSST footprint are performed exactly as for single stars, assuming the same stellar density profiles, and that all stars are in binaries drawn from the Eggleton (2006) distribution of initial parameters (including the mass ratio and orbit). However, because of the higher computational cost with respect to single-star simulations, we computed only one-tenth of the binaries expected from such stellar density profiles. Anyway, the catalogs for single and binary stars can be combined, a posteriori, by sampling the stars from the two distributions, as discussed in Section 3.2.

2.4. Single Stars in the Magellanic Clouds

The Magellanic Clouds are simulated separately from the MW, as objects added at fixed distance and with their own star formation history (SFH),[14] distance, and extinction.

For the SMC, we adopt the space-resolved SFH, distance and extinction together with 1σ uncertainties, derived by Rubele et al. (2015) from near-infrared data from the Visible and Infrared Survey Telescope for Astronomy (VISTA) Survey of the Magellanic Clouds (VMC; Cioni et al. 2011). These SFH maps comprise a total area of 23.57 deg^2 around the main body of the SMC and represent the analysis of 168 subregions each one with an area of $\sim$0.143 deg^2.

The simulation uses the same grids of stellar models as for the Milky Way but adopts the IMF from Kroupa (2002), because this ensures consistency with the previous work of derivation of the SFH by Rubele et al. (2015). This consistency is not complete, however, as we do not include the binaries in

[14] In general, the SFH is made by the combination of a star formation rate as a function of the age, SFR (t), and age–metallicity relation (AMR), [Fe/H](t).

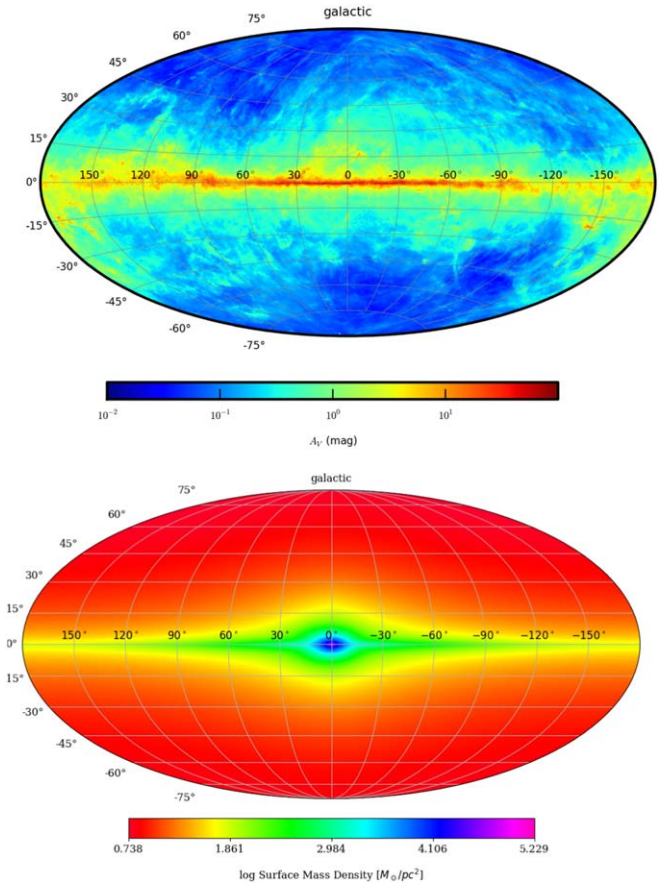

Figure 1. The two maps that define how the sky is split into smaller areas: the extinction map derived from (Planck Collaboration et al. 2014, top panel) and the surface mass density derived from the Girardi et al. (2012) calibration of TRILEGAL (bottom panel).

the same way as Rubele et al. (2015). In their case, binaries are built by adding, to 30% of the stars drawn from the IMF, an unresolved companion taken from the same isochrone and with an initial mass ratio randomly chosen in the interval from 0.7 to 1. This prescription means that our simulation of single stars contain about the same star counts as Rubele et al. (2015), but they lack the specific features caused by apparent binaries in the CMD: essentially, they lack a broadened MS and a small fraction of scattered giants, brighter than single stars by 0.7 mag at most. This difference can be made up by adopting a reasonable fraction of binaries, as discussed later in Section 3.2.

As for the LMC, the SFH comes from the comprehensive work by Harris & Zaritsky (2009). They derive the SFH for 386 regions of $\sim$0.16 deg^2 and covering a total area of $\sim$ 62 deg^2. They provide the interstellar extinction for each star used in the SFH analysis, differentiating between younger hot stars and older cool stars. Starting from the two reddening maps of hot and cool stars, we derive the corresponding mean reddening values $A_{V,i}^{\rm Hot}$ and $A_{V,i}^{\rm Cool}$ for each LMC region i, and finally adopt the mean between these values.

We assume the LMC center has a true distance modulus of 18.5 mag. According to van der Marel & Cioni (2001), the LMC stellar populations are distributed in a disk with an inclination of $34\overset{\circ}{.}7$ with the respect to the plane of the sky, implying changes in the distance modulus amounting to $\sim$0.1 mag. We take this geometry into account, by adjusting the distance modulus of each region (Harris & Zaritsky 2009; see their Section 3.4 for details).

Table 2
All Possible Stellar Kinds in BinaPSE (and BSE)

k	Stellar Kind
0	Main sequence (MS) and fully convective
1	MS and not fully convective
2	Hertzsprung gap (HG)
3	Giant branch (GB)
4	Core helium burning (CHeB)
5	Early asymptotic giant branch (EAGB)
6	Thermally pulsing AGB (TP-AGB)
7	Naked helium star MS (HeMS)
8	Naked helium star HG (HeHG)
9	Naked helium star GB (HeGB)
10	Helium white dwarf (He-WD)
11	Carbon–oxygen white dwarf (CO-WD)
12	Oxygen–neon white dwarf (ONe-WD)
13	Neutron star (NS)
14	Black hole (BH)
15	Massless remnant

As the LMC simulation comes from SFH maps derived with different stellar models and IMF, a final step is necessary to ensure that TRILEGAL produces the correct, observed numbers of LMC stars, out of the Harris & Zaritsky (2009) tables. To check on this, we produce a TRILEGAL simulation for each single region in the Two Micron All Sky Survey (2MASS) $JHK_{\rm s}$ filters. We then compare the predicted and observed star counts in a region of the $K_{\rm s}$ versus $J-K_{\rm s}$ CMD that is dominated by LMC RGB stars and is little affected by saturation or incompleteness in the 2MASS data, namely, the box defined by $13 < K_{\rm s} < 14$ and $0.7 < J-K_{\rm s} < 1.3$. We find that, when using a Kroupa (2002) IMF in place of the Salpeter IMF originally used by HZ09, the predicted numbers of RGB stars match the observed ones within a 3σ difference, except for a few outliers. The absence of any strong difference in the star counts—and hence the nonnecessity to apply any "normalization constant" in present models—is confirmed by the new SFH maps derived by Mazzi et al. (2021).

Once the simulations are done, we randomly add sky coordinates for all the stars within each field. Then according to their coordinates each simulated star is assigned to the correspondent HEALPix pixel in the MW simulation (which, across the Magellanic Clouds, is computed with $n_{\rm side} = 128$).

Figure 2 shows the CMD for the LMC, SMC, and their MW foreground. The predicted number counts for each evolutionary phase are listed in Table 3.

Importantly, the LMC and SMC simulations include only the area covered in present SFH maps. As a consequence, these galaxies appear with a nearly rectangular shape in the stellar density maps of Figure 3.

2.5. Binaries in the Magellanic Clouds

Like for MW regions, the simulations of binaries in the Magellanic Clouds are performed exactly as for single stars, assuming the same SFHs, and we computed only one-tenth of the expected binaries.

3. Available Data

To summarize, we built two large simulated catalogs: the first containing single stars in the MW and Magellanic Clouds, the second containing just their binaries with stellar counts

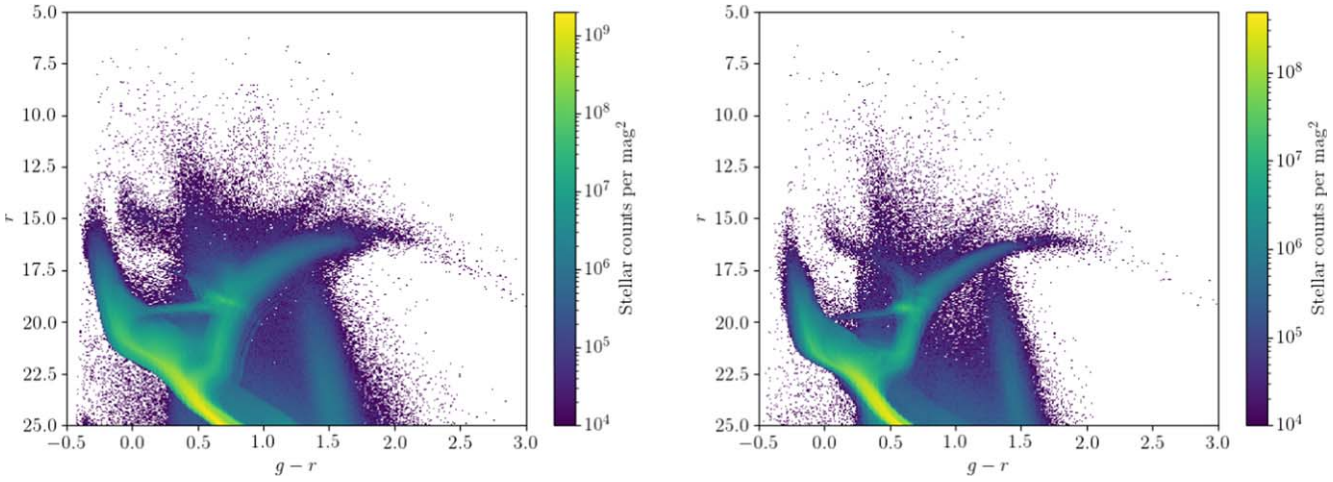

Figure 2. CMD (r vs. $g-r$) of the simulated number density per mag^2 of the Magellanic Clouds (LMC and SMC, left and right panels, respectively) and the corresponding MW foreground. These are Hess diagrams, with the color scale illustrating the counts of stars in small color–magnitude bins. In the less populated regions of the CMD these stellar densities are replaced by a simple scatter plot of the simulated stars. The MW foreground appears mainly as two almost-vertical features: a marked one at $g-r \simeq 1.5$, and a more diffuse one located just redward of $g-r=0.3$ mag (partially overlapping the He-burning and main sequences of the Magellanic Clouds).

Table 3
Predicted Number Counts for Each Evolutionary Phase from the MW, LMC, and SMC Simulations of Single Stars, Down to the $r=27.5$ mag Limit

Stage	MW (10^6)	LMC (10^6)	SMC (10^6)
PMS	635.7	4.3	1.2
MS	9275.1	81.1	33.9
SG	275.6	3.6	2.2
RGB	139.0	2.2	1.2
CHeB	156.3	2.3	0.2
EAGB	6.92	0.2	0.1
TPAGB	0.44	0.03	0.009
Post-AGB + WD	101.5	2.1	1.6
Total	10489.1	95.8	40.4

reduced by a factor of one-tenth. In the following, we will simply refer to these catalogs as the $f_{\rm bin}=0$ and $f_{\rm bin}=1$ cases, respectively. We will mainly discuss the results obtained with the $f_{\rm bin}=0$ catalog.

3.1. The Full Catalog in Data Lab

The full catalogs containing 10.6 billion single stars and 1.61 billion binary systems are made available at the NOIRLab Astro Data Lab (Olsen et al. 2019) and named as `lsst_sim.simdr2`[15] and `lsst_sim.simdr2_binary`,[16] respectively. All the quantities stored are reported in Tables 4 and 5.

The resulting stellar density, i.e., stellar counts per square degree, for $f_{\rm bin}=0$ and variable resolution, is shown in Figure 3.

3.2. Combining Single and Binary Models

As described above, we have single and binary catalogs that should be combined in to provide a realistic description of real stellar populations. Unfortunately there is still substantial uncertainty about how they should be combined. Several aspects should be considered.

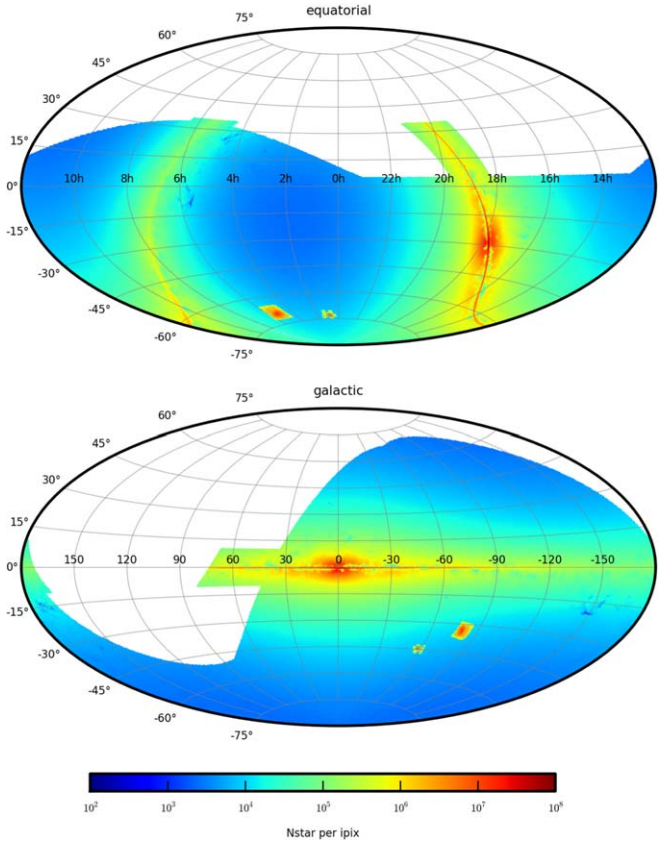

Figure 3. Stellar density (star counts at $r<27.5$ mag per square degree) in the LSST simulation with $f_{\rm bin}=0$, in both equatorial and Galactic coordinates (Aitoff projection).

First, we should recall how the densities of MW populations were calibrated in the `TRILEGAL` code (see Girardi et al. 2005, 2012): In that process, we were using models composed of single stars but adding a stellar companion to 30% of them. Such binaries did not interact, they had a flat distribution of mass ratios between 0.7 and 1, and the masses of the companions were (erroneously) not considered in the total population mass. In other words, the main effect of adding the

[15] https://datalab.noirlab.edu/query.php?name=lsst_sim.simdr2
[16] https://datalab.noirlab.edu/query.php?name=lsst_sim.simdr2_binary

Table 4
Quantities Stored in the Astro Data Lab for Single Stars

Quantity	Description
gall, galb	Galactic latitude and longitude in degrees.
Gc	Galactic component the star belongs to: 1 → thin disk; 2 → thick disk; 3 → halo; 4 → bulge; 5 → Magellanic Clouds.
logAge	Logarithm of the stellar age measured in years.
M_H	Metallicity [M/H].
m_ini	Initial mass in $M_{\odot}$.
mu0	True distance modulus, μ_0 or $(m - M)_0$.
Av	Extinction in the Johnson's V band, A_V.
Mass	Current stellar mass in $M_{\odot}$.
logL	Logarithm of the luminosity in $L_{\odot}$.
logTe	Logarithm of the effective temperature in kelvin.
logg	Logarithm of surface gravity g in cm s^{-2}.
label	Evolutionary phase of the star, as in Table 1.
McoreTP	Core mass during the TP-AGB phase in $M_{\odot}$.
C_O	Surface abundance ratio by number, n_C/n_O, during the TP-AGB phase.
period0, period1, period2, period3, period4	Periods for classical Cepheids and LPVs, in days, in the fundamental and 1st, 2nd, 3rd, and 4th overtone modes, respectively. Cepheids contain only period0, period1. Values are set to 0 for the other stars.
pmode	Radial order of the dominant pulsation mode, (0 is the fundamental mode, 1 is the 1st overtone mode, and so on). It has value 0 or 1 for classical Cepheids, from 0 to 4 for LPVs, and is set to −1 for the other stars.
Mloss	Mass-loss rate in $M_{\odot}$ yr^{-1}.
tau1m	Optical depth of circumstellar dust at $\lambda = 1$ μm.
X, Y, Xc, Xn, Xo	Abundances of H, He, C, N, and O, respectively.
Cexcess	Carbon excess in atmosphere of C-rich stars, defined as $C - O = \log(n_C - n_O) - \log(n_H) + 12$. It is set to −1 for O-rich stars.
Z	Surface metal content, Z.
mbolmag	Absolute bolometric magnitude.
umag, gmag, rmag, imag, zmag, ymag, Gmag, G_BPmag, G_RPmag	Apparent magnitudes in the LSST (u, g, r, i, z, y) and Gaia (G, G_{BP}, G_{RP}) photometric systems.
velU, velV, velW	Galactocentric velocities U, V, W in kilometers per second.
Vrad	Radial velocity in kilometers per second.
PMracosd, PMdec	Proper motions along the equatorial coordinates (α, δ) in arcseconds yr^{-1}.

Note. Data can be found at https://datalab.noirlab.edu/query.php? data-cke-saved-name=lsst_sim.simdr2.name=lsst_sim.simdr2.

stellar companions was that of modestly increasing the stellar luminosities and making broader main sequences, with hardly any consequence to the total star counts or MW densities.

The new scheme for simulating binaries introduced in Dal Tio et al. (2021), instead, produces both noninteracting and interacting binaries, with a more realistic distribution of mass ratios (and also orbital parameters), and in numbers defined by the population initial total mass. To reproduce a given stellar density using single and binary models, this scheme requires the specification of a suitable initial binary fraction (by mass), f_{bin}. Preliminary work on Gaia Data Release (DR) 2 data within 200 pc (Dal Tio et al. 2021) indicates f_{bin} values of about 0.4 when the shape of the lower main sequence is fitted, but favors values as large as 0.9 when fitting the intrinsically brightest and more massive stars. This uncertainty about the best value of f_{bin} might not be solved before Gaia DR3, when a more detailed analysis of the nearby binaries will become possible.

That said, the present computation of binary systems represents just one-tenth of the binaries that should be in a "binaries-only" simulation. To create a $f_{bin} = 1$ simulation, the binary counts presently tabulated should be multiplied by a factor 10.

Let us now take a look at the stellar counts produced by $f_{bin} = 0$ and $f_{bin} = 1$ models. They are illustrated in Figure 4 for the case stars close to the SGP. For this figure and for the example in Section 4.1 we actually simulated all binary systems expected in the SGP, not just one-tenth. As can be noticed, over a very wide interval in brightness—$r < 21$ mag, which is the most relevant in the original calibration of TRILEGAL parameters—there is just a modest deficit, of between 7% and 9%, in the star counts of $f_{bin} = 1$ models, compared to the $f_{bin} = 0$ ones. The modest value of this deficit suggests that the simple adoption of the f_{bin} scheme devised by Dal Tio et al. (2021) is acceptable, as a first approach: when used together with MW densities calibrated in the original scheme, it will produce star counts just a few percent different from the previous ones. In other words, no dramatic recalibration of TRILEGAL density parameters is required if we adopt the f_{bin} scheme to combine single and binary catalogs. We also note that the "deficit" of binaries in Figure 4 increases to ∼30% at the faintest magnitudes ($r \gtrsim 25$ mag); this however is a regime dominated by very-low-mass cool dwarfs located close to the Sun, whose probability of being observed as two resolved stars (and not as a single binary) is increased with respect to the brighter sample. This effect would reduce their "deficit" by a quantity that is still to be evaluated for LSST—following, for instance, the same approach used by Dal Tio et al. (2021) in the case of Gaia DR2 data.

Therefore, for the moment, we recommend a f_{bin} value of 0.4, as being both most robust (see Dal Tio et al. 2021) and more consistent with the way the stellar densities were originally calibrated in TRILEGAL. As we simulated only one-tenth of expected binaries, the f_{bin} value of 0.4 can be achieved by randomly selecting 60% of single stars and by multiplying by 4 times the number of binary systems present in the same regions.

Table 5
Additional Quantities Stored in the Astro Data Lab for Binary Stars

Quantity	Description
ID	Identification number of the binary system.
c1_KW, c2_KW	Stellar types (as in Table 2).
P	Current orbital period in days.[a]
a	Current semimajor axis in $R_\odot$.[a]
e	Current eccentricity.[a]
i	Inclination of the orbit in degrees.
K1, K2	Radial velocity amplitudes in $R_\odot$/days.[a]
Delta_r1, Delta_r2	Maximum depth of the primary and secondary eclipses, in magnitudes, in the r band.[b]

Notes. Quantities for primaries and secondaries are already described in Table 4, and they are not repeated here; suffice it to mention that they are now preceded by the prefixes c1_ and c2_, respectively. The photometry is presented also for the total binary system, preceded by the prefix c3_. The coordinates, distances, and space velocities, as described in Table 4, refer to the center of mass. Data can be found at https://datalab.noirlab.edu/query.php?data-cke-saved-name=lsst_sim.simdr2_binary.name=lsst_sim.simdr2_binary.
[a] P = 0, a = 0, e = −1 for merged binaries.
[b] 0.0 if no eclipse occurs.

Future versions of our simulations will adopt more consistent approaches and have simpler recommendations. Fortunately, the $f_{\rm bin} = 0$ models are also good enough for simple applications related with star counts, as those illustrated in the following.

3.3. The Stellar Density Files in MAF

A basic requirement of the LSST simulations is the possibility of quickly estimating the expected stellar numbers as a function of both the location in the sky and of the brightness in any of the survey passbands. Such numbers are referred to here as either "stellar density files" or "luminosity functions" (LF). They are extensively used on MAF, in the form of two-dimensional matrices containing the expected star counts per healpix in the sky and per magnitude bin, for all six LSST filters. Their resolution is usually of $n_{\rm side} = 64$ and 0.1 mag, which ensures that data files are small enough to be distributed via github and to be quickly read and processed by any part of the MAF software. Most recent applications, however, also required the calculation of such files for $n_{\rm side}$ values up to 1024.

We derive such LF plus stellar density files from our simulations of single stars ($f_{\rm bin} = 0$). For each pixel in the simulation, we computed the LF for all LSST and Gaia filters, using 0.2 mag wide bins in the magnitude range from 15.0 to 28.0. Different pixels were then added together, or split into subpixels, to produce the LFs for uniform pixelations ranging from $n_{\rm side} = 64$ to $n_{\rm side} = 1024$.

These luminosity functions plus stellar density maps were added to the software used by MAF, starting from the lsst_sims version tagged sims_w_2020_05. They can be easily activated in place of the previous galfast maps. In general, the usage of these specific MAF files can be easily spotted by the presence of the Magellanic Clouds (which were absent in the galfast simulations) in any of the derived sky maps, provided that such maps are sensitive to the stellar density.

To assist in the latest efforts of cadence optimization, these maps were expanded so as to include the entire footprint up to $\delta < 40°$. This extension was, however, made on a fast and approximate way, with respect to the full simulation above described. More specifically, the extension was done using an uniform resolution of $n_{\rm side} = 64$, and reducing the stellar densities internally used by TRILEGAL by a large constant factor; this artificial reduction in densities was later taken into account to derive the final LFs. This means that the star counts predicted for this extended area are noisier (at both the spatial and brightness scales) than in the main simulation described above in Section 3.1—but still they are well suited to explore the possible extension of the WFD survey to northern sky areas.

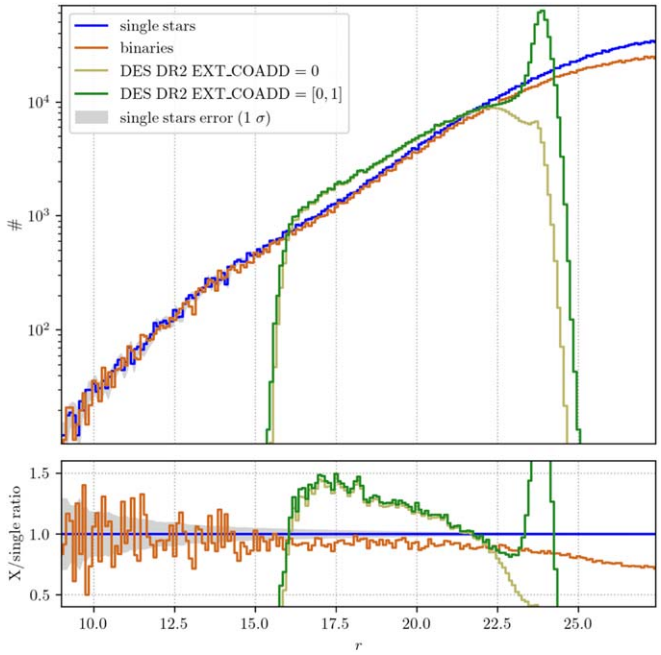

Figure 4. Top panel: LFs in the r band for stars within 5° of the SGP, for both single and binary stars (that is, for the $f_{\rm bin} = 0$ and $f_{\rm bin} = 1$ simulations, respectively). The bottom panel shows the ratio between the $f_{\rm bin} = 1$ and $f_{\rm bin} = 0$ simulation. In addition, both panels present the real LFs derived from DES data, to be discussed in Section 4.1 below: one of them is more conservative (EXT_COADD = 0), and the other one more complete (EXT_COADD = [0,1]). For the sake of comparison, the gray shaded area shows the Poisson noise expected in the case of single stars; this noise becomes negligible in the magnitude interval covered by the DES data.

4. Examples and Applications

In this section we illustrate some properties of our simulation and some of the aspects useful to plan LSST surveys.

Before proceeding, we recall that TRILEGAL has been checked and calibrated against many different data over the years. While we are sure that it performs well—with errors in stars counts of the order of ∼20%—for optical-near-infrared shallow surveys, and for a few deep small-area surveys, its performance with deep surveys covering huge areas is still to be verified. There is ongoing work to improve the description of the different MW components, as for instance (1) the fine-tuning of structural parameters of the thick disk and halo using deep data from the Dark Energy Survey for high-latitude fields (Pieres et al. 2020); (2) the fitting of the spatially varying SFH of the nearby thin disk recently made possible by Gaia DR2 +EDR3 (following the initial work by Dal Tio et al. 2021), and (3) the fitting of bulge structural parameters using data from VISTA Variables in the Via Lactea (VVV; A. Mazzi et al. 2022, in preparation). Such recalibration work is not yet incorporated in the present work.

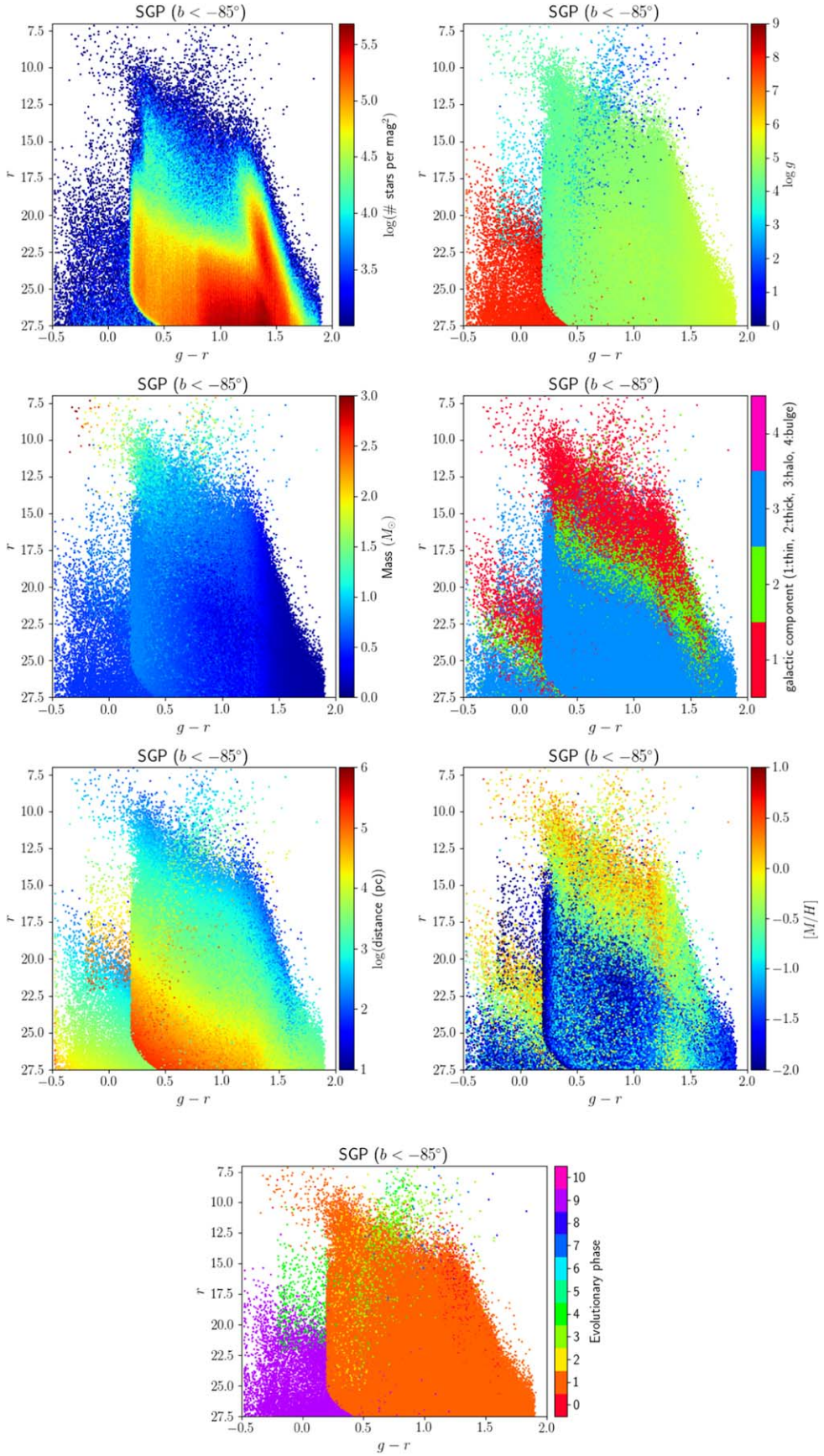

Figure 5. Top-left panel shows the CMD (or Hess diagram) for all simulated single stars in the $n_{\rm side} = 64$ pixels whose centers lie within 5° of the South Galactic Pole (SGP). Subsequent panels present their distributions of surface gravity, initial mass, Galactic components, distances, metallicity, and evolutionary phase.

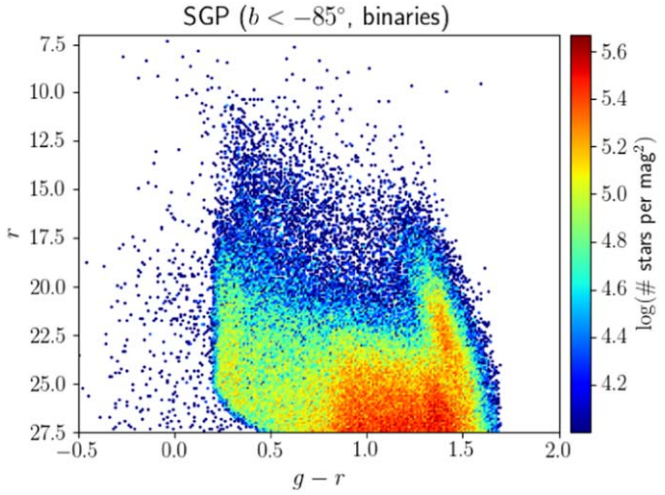

Figure 6. CMD for all simulated binaries in the $n_{\rm side} = 64$ pixels whose centers lie within 5° of the South Galactic Pole (SGP). Their distributions of galactic components, distances, and metallicities are similar to those in Figure 5.

4.1. Example 1: The South Galactic Pole

Figure 5 shows the r versus $g - r$ CMD for all 1,407,759 single stars in the $n_{\rm side} = 64$ pixels whose centers lie within 5° of the South Galactic Pole (SGP). The several panels color code the stars according to some of their properties (distance, metallicity, $\log g$, etc). It can be noticed that

1. the bulk of stars are dwarfs, with some contribution from giants at $r \lesssim 15$, $g - r \gtrsim 0.5$, and white dwarfs at $r \gtrsim 20$, $g - r \lesssim 1.0$;
2. the most prominent nearly vertical features correspond to the thick disk and halo turnoffs at $g - r < 0.5$, and to the onset of low-mass M dwarfs and $g - r \approx 1.5$;
3. most of the dwarfs are long-lived stars of masses $M \lessapprox 1$ $M_\odot$; as a consequence, they uniformly sample the age range and original metallicities of their parent populations;
4. the bluest dwarfs essentially disappear at $r > 25$, simply because the halo becomes too sparse for distances larger than ≈50 kpc; the only stars expected at such faint magnitudes and blue colors, are white dwarfs.

Figure 6 shows the CMD for the binaries, assuming they are all unresolved. Their distributions of parameters such as distance and metallicity are similar to those of single stars. We remind that, for this example, we simulated all expected binary systems and not only one-tenth as in the public catalog.

Figure 7 instead shows the $g - r$ versus $u - g$ CCD for the same SGP simulation, assuming that every star observed in g and r bands is also observed in u. Although this latter assumption is not very realistic, the plot confirms that the simulation presents the correct (observed) behavior for the stars as a function of parameters such as metallicity and $\log g$ (see, e.g., Ivezić et al. 2008 for G-K dwarfs and giants, and Bianchi et al. 2011; Rebassa-Mansergas et al. 2013 for WDs).

In any case the simulations also present some discontinuities likely associated to the heterogeneous libraries of model atmospheres we have used, especially at the cool end of the $T_{\rm eff}$-color relations. You can see for instance that the $u - g$ sequence bifurcates for $g - r > 1.5$: the subsequence going up at slightly decreasing $u - g$ comprehends all stars with $T_{\rm eff} < 2800$ K, and occurs because we only have solar-metallicity model spectra at the cool end of the $T_{\rm eff}$ scale. So, we prefer to have the coolest metal-poor dwarfs simulated with colors and magnitudes that are probably off by some tenths of magnitudes, rather than not simulating them at all. Of course, predicted star counts for very-low-mass stars should be considered as highly uncertain, also taking into consideration the uncertainties in the low-mass IMF.

Figure 8 shows the CCD for the binaries, assuming they are all unresolved. Comparison with the same plot for single stars in Figure 7 reveals that binaries are responsible for some of the most deviant points with respect to the main CCD sequences. Most remarkably, they explain the many stars that appear with a $u - g$ bluer than the main sequence in the CCD: these are, generally, MS or red giant stars with a evolved hot companion (including WDs, HBs, and hot subdwarfs).

Figure 4 also includes a comparison between our simulations and real stars from DR2 of the Dark Energy Survey (DES). Two samples of stars were selected from that release, using the morphological classifier `EXT_COADD`. DES DR2 `EXT_COADD = 0` selects a pure sample of stars (even incomplete), while in DES DR2 `EXT_COADD = [0,1]` includes more sources with photometric shapes similar to PSFs, but with an expected contamination of galaxies, mainly quasi-stellar objects (QSO) close to $r \sim 24$ mag. We refer to Abbott et al. (2021) for a detailed discussion about the `EXT_COADD` classifier.

The area in the sample of DES stars covers 5° of the SGP and two objects were masked in this region: the globular cluster NGC 288 and the galaxy NGC 253. The histogram in Figure 4 is corrected by the coverage area, when removing the stars closer than $0\overset{\circ}{.}5$ and $0\overset{\circ}{.}25$ around these objects, respectively. Limiting the discussion to the interval not affected by saturation ($r \gtrsim 16$), the bottom panel of Figure 4 shows that there are 50% more stars than simulated in the interval $16 < r < 21$. This deficit of simulated stars disappears at $r \sim 22$, becoming a slight excess at $r = 23$. As the classifier is not able to distinguish between stars and QSOs, there is a sensible increase in the star counts close to $r = 24$ in the sample of DES stars with `EXT_COADD=[0,1]`, while the sample of more pure stars monotonically decreases after $r = 22.5$. The reader should keep in mind that similar discrepancies in the star counts are likely to be present at other sky regions that mostly sample the thick disk and halo of the MW.

4.2. Example 2: Bulge and Inner Disk Fields

The Galactic bulge forms a particularly challenging test for population synthesis models. It is intrinsically complex, with even the spatial distribution appearing to depend on the sample of tracers used (with younger and/or more metal-rich populations defining a narrower bar structure; e.g., Catchpole et al. 2016; Portail et al. 2017a, 2017b; Grady et al. 2020; Lian et al. 2021). The bulge is also an *observationally* challenging region, with a high degree of spatial confusion at the faint end and a plentiful foreground of objects bright enough to produce charge bleeds and other artifacts in CCD exposures that are sufficiently sensitive to measure faint populations (see Schlafly et al. 2018 for discussion of both effects). Furthermore, the bulge is subject to strong extinction, with rapid spatial variation, and for which the reddening law is strongly suspected not to follow standard prescriptions and is likely itself spatially variable (e.g., Nataf et al. 2016; Saha et al. 2019). These factors *increase* the need for a trustable

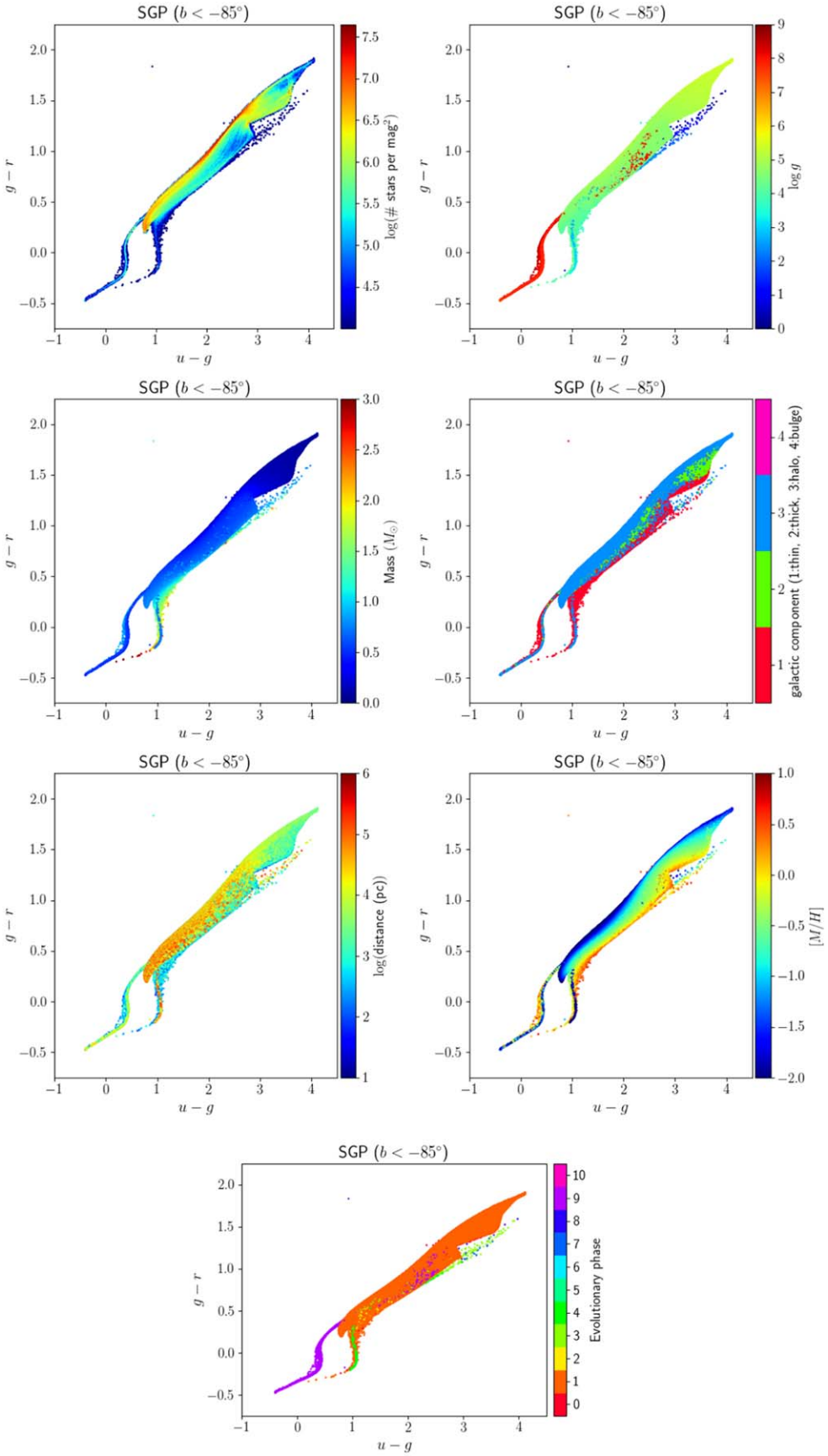

Figure 7. CCD for all simulated single stars in the $n_{\rm side} = 64$ pixels whose centers lie within 5° of the South Galactic Pole (SGP). Stars are color coded as in Figure 5.

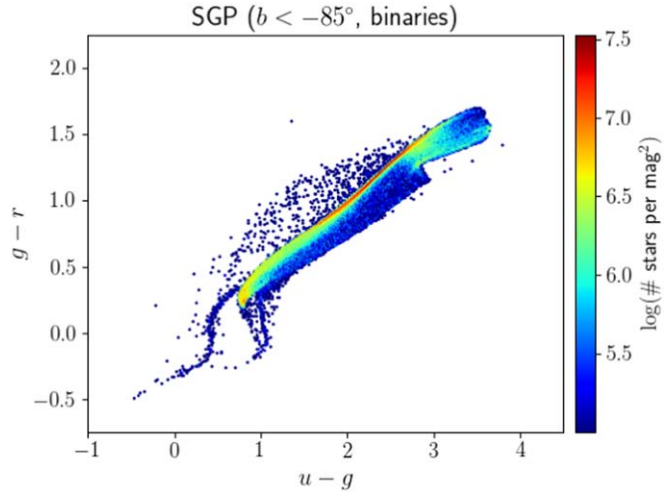

Figure 8. CCD for all simulated binary stars in the $n_{\rm side} = 64$ pixels whose centers lie within 5° of the South Galactic Pole (SGP).

simulation toward bulge regions for the purposes of observation planning and assessment, and so we present here the comparison of TRILEGAL predictions with bulge fields selected to include a wide range of observed stellar densities and/or extinction and reddening effects.

Figure 9 and Table 6 present the fields chosen for the comparison. The well-studied Baade's Window region (field baade) was chosen to probe the inner bulge in a region likely to reach the seeing-limited confusion limit. A second field, VVV372, was chosen to provide coverage of a dense higher-extinction region for which near-infrared photometry is publicly available (as it is with the Baade's Window region). The remaining fields step out along the bulge/bar and thin, thick disks at regular intervals in (negative) Galactic longitude. Fields as far out as disk2 and possibly even disk3 likely contain substantial contributions from the bulge/bar system itself (see Wegg et al. 2015), while the far two fields, disk6 and disk7, probe regions of moderate and low extinction beyond the solar circle. The fields are each nominally $1° \times 1°$ in size, and no field samples closer to the Galactic midplane than $|b| < 1.°5$, because we surely do not trust our model predictions in detail so close to the midplane.

The fields toward the inner bulge and disk are characterized by rapid variations in stellar density and extinction. The latter is evident from the extinction map presented in Figure 9 and contributes to cause the strong spatial variation in the stellar density of our simulations. Given the simplicity with which we describe 3D stellar density and extinction in TRILEGAL, significant differences between models and observations can be expected for these areas. Also, we recall that the current models for the bulge region are based on the calibration work performed by Vanhollebeke et al. (2009), using 2MASS and Optical Gravitational Lensing Experiment (OGLE) data regarding relatively bright stars ($K_s < 11$ and $I < 14$, respectively), for low-reddening regions only, and with no subselection on tracer population (see Grady et al. 2020). It is far from obvious that such a model can be extrapolated to describe very deep observations across the entire bulge. In addition, TRILEGAL assumes a slowly varying distribution of extinction along the line of sight, whereas in reality the extinction is likely to be concentrated in a few distances (e.g., Bovy et al. 2016; Green et al. 2019; Lallement et al. 2019). Thus, the comparison of the *current* model serves to inform the end user of the degree to which the predictions match deep seeing-limited data and to highlight areas in which further improvement can be expected.

For observational comparison, we choose the DECam Plane Survey (DECaPS; Schlafly et al. 2018), which presents publicly available photometry in the DECam (*grizY*) bandpasses, over a wide region of the inner plane ($|b| \lesssim 4°$, $-120 \lesssim l \lesssim +5°$) and which therefore encompasses all our chosen comparison fields. For two fields, baade and VVV372, near-IR ($ZYJHK_s$) photometry is available via the VVV (Minniti et al. 2010) survey.

This work uses the DECaPSv1 merged source catalog (Schlafly et al. 2018),[17] which does not include quality flags on its average magnitudes. Although only "good" objects are included in DECaPSv1 (Schlafly et al. 2018), we found many obvious artifacts around bright objects (e.g., strings of objects along diffraction spikes of very bright objects), and extremely bright objects themselves do not appear in the catalog (leading to erosion of the bright end of the observed LF). Systematic correction for these artifacts is beyond the scope of this work; we simply selected spatial regions that avoided the brightest objects. For at least one field (disk6), this removed substantial spurious features in the LF.

Figure 10 compares the CMDs (in g, r) between DECaPS and our simulations, for the innermost and outermost comparison fields, baade and disk7 (the same comparison for the rest of the comparison fields can be found in Appendix C). They give an overview of the main features expected in these fields. First, we have the blue main sequence stretching from very bright to very faint brightness, which mainly represents the thin disk along the entire line of sight, and is present in all fields. Second, we have a few extended features at the red part of the diagram, the main one being a diagonal strip caused by red clump stars; these red sequences are very prominent over the bulge and just hinted at in the case of the disk7 field.

Figure 11 presents the comparison between the LFs predicted by TRILEGAL against DECaPS and galfast, for all fields shown in Figure 9, arranged in increasing Galactic longitude (i.e., increasing distance from the minor axis). In the low-extinction baade field (and only in this field), the red clump is unambiguously apparent in all filters, allowing some sensitivity to shifts in both number count and the apparent magnitude at which a given feature appears. In this field, the TRILEGAL LF shows similar morphology to the DECaPS LF, but it is shifted fainter than the DECaPS LF by about 0.7 mag in g, with the difference decreasing toward longer-wavelength filters. The outermost fields disk6 and disk7 show close agreement between model and data, despite showing much higher extinction than is apparent in baade (Table 6). In the intermediate fields, TRILEGAL often underpredicts the number counts, by about a factor of 2–3 (though again the broad morphology of the TRILEGAL LF prediction is similar to that observed in DECaPS).

We quantify the discrepancy between data and model LFs in order to examine it as a function of the total extinction A_V and of the Galactic coordinates of the comparison samples. The discrepancy is quantified as

$$S = M/N, \tag{1}$$

[17] http://decaps.skymaps.info/catalogs.html

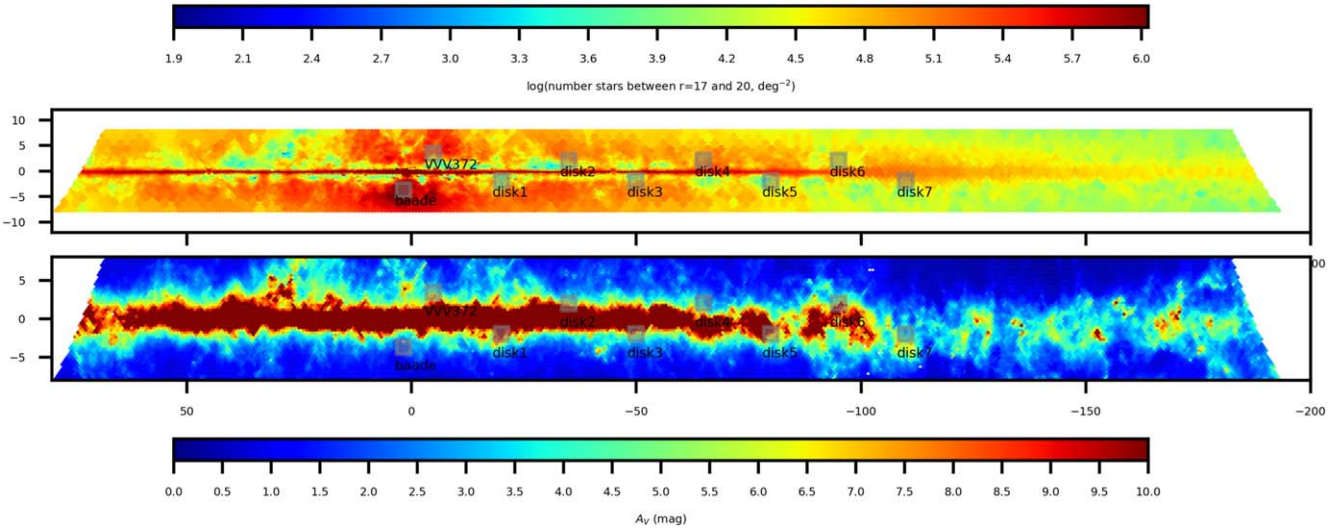

Figure 9. Top panel: simulated stellar density for the stars with $17 < r < 20$, for the Galactic plane and bulge areas. The squares are areas for which we are checking the star counts with DECaPS data (see Figures 10 and 11 below). Bottom panel: extinction A_V derived from Planck maps. All regions with $A_V > 10$ mag appear in dark red. See Section 4.2.

Table 6
Comparison Fields Chosen for the Bulge and Inner Disk

				$S = M/N$ in									
Field Name	l	b	A_V	g	r	i	z	y	Z	Y	J	H	K_s
baade	+1.7	−3.7	2.1	0.52	0.45	0.47	0.49	0.56	0.47	0.49	0.53	0.56	0.54
VVV372	−4.9	3.4	5.44	0.44	0.51	0.43	0.42	0.46	0.39	0.40	0.41	0.44	0.42
disk1	−20.0	−2.0	11.87	0.35	0.32	0.34	0.33	0.35	…	…	…	…	…
disk2	−35.0	2.0	7.37	0.52	0.42	0.39	0.38	0.37	…	…	…	…	…
disk3	−50.0	−2.0	7.96	0.25	0.26	0.26	0.28	0.27	…	…	…	…	…
disk4	−65.0	2.0	3.68	0.53	0.52	0.52	0.54	0.51	…	…	…	…	…
disk5	−80.0	−2.0	9.04	0.25	0.29	0.32	0.36	0.37	…	…	…	…	…
disk6[a]	−95.0	2.0	8.26	0.98	0.93	0.97	0.98	0.94	…	…	…	…	…
disk7	−110.0	−2.0	3.74	0.81	0.87	0.80	0.82	0.81	…	…	…	…	…

Notes. Reading left to right, columns give the field name, the Galactic longitude and latitude of the center of each 1° × 1° field, and the mean (V band) extinction according to the Planck extinction map (Planck Collaboration et al. 2014) in each field. The bulge/bar contribution is likely mostly interior to $|l| \lesssim 30°$ (e.g., Wegg et al. 2015). See Section 4.2 and Figure 9.

[a] DECaPS data for disk6 have been cut to avoid a large defect due to a very bright and saturated star. Its true extension in longitude is $264.0 < l < 265.77$. The LF of the simulation is rescaled by a factor 0.885 to reflect this reduced area.

where N, M are the observed counts over the range ($15 \leqslant g < g_{\rm max}$) for the observed sample and TRILEGAL, respectively. The magnitude limits are chosen to minimize the impact of observational incompleteness. The bright limit of $g_{\rm min}$=15 is set by inspection of the DECaPS saturation limit on the giant branch for the fields of interest. The faint limit is set dynamically for each field to minimize the impact of incompleteness in the observed catalog at the faint end: $g_{\rm max}$ is the peak of the g-band apparent magnitude histogram, or $g_{\rm max} = 23$, whichever is *brighter*. The same selection is used for the discrepancy estimate in all filters (i.e., the sample selected by the g-band apparent magnitude is used for all filters) using as bright magnitude limit 15 for the DECaPS filters and 14 for the VVV ones. While the discrepancy measures are tabulated for all the filters (Table 6), we use the discrepancy in g to assess the mismatch here.

Figure 12 shows the results. We note that TRILEGAL currently underpredicts the total star counts in all the fields. Fields disk6 and disk7, which are the farthest from the rotation axis, show the smallest discrepancy between simulation and model, with the closest - disk6 - showing better than 90% of the observed star counts in all the DECaPS filters. Indeed, these two fields (both outside the solar circle) seem to show qualitatively better agreement than the fields at $|l| \lesssim 90°$ (Figure 12, top panel), despite these high-longitude fields not lying at the extremes of the extinction distribution (Figure 12, bottom panel). As these are also the fields at which the intrinsic contribution of the bulge/bar itself is expected to be negligible, we can view these fields as a control test against which the inner Milky Way is probed over the rest of the fields. When these two fields are excluded, then, we see that TRILEGAL tends to underpredict the raw counts in the observations by a factor ∼2–4, depending on the field and filter (note that disk3, beyond the far tip of the bar, is the field showing the lowest discrepancy in total counts, and *not* baade). Again excluding disk6 and disk7, a noisy trend against A_V may be present. If there is a trend against Galactic longitude, it does not appear to be simple or monotonic.

At this time we cannot draw conclusions about whether the discrepancies between TRILEGAL and observations are driven

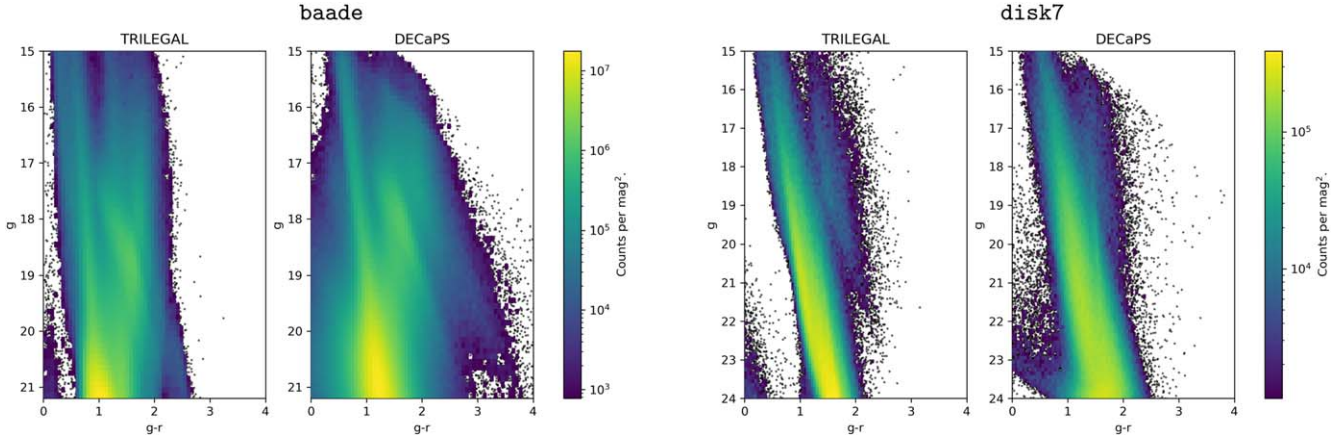

Figure 10. Comparison between TRILEGAL and DECaPS CMDs (or Hess diagrams), for two of the areas drawn in Figure 9, namely, baade (which corresponds to Baade's Window; left panels) and disk7 (right panels). Additional plots are presented in Appendix C. See Section 4.2.

mainly by extinction or by approximations in the structural model itself. However, a comparison with VVV data suggests that reddening complications must be an important contributor to the discrepancies, at least in baade and VVV372, the two fields for which the comparison is currently possible.[18] Figure 13 shows the results for the CMDs, while Figure 14 shows the LFs. In field baade, the red clump appears about $\Delta K_s \approx +0.12$ mag fainter in TRILEGAL than in the VVV data. Comparison of this offset between the K_s and g filters suggests the LF discrepancy is probably at least partly driven by extinction, because at $\Delta g/\Delta K_s \sim 1.0/0.12 \approx 8$ the apparent magnitude shifts in the two filters are more discrepant than would be expected by distance effects alone. Field VVV372 also shows a smaller shift in red clump apparent magnitude at K_s than in the bluer filters, although for that field the comparison is more difficult to draw at shorter wavelengths.

Indications are therefore that the TRILEGAL number counts currently underpredict the true star counts in deep seeing-limited observations by a factor ~2 in (*grizY*) for bulge regions with $A_V \lesssim 8$ and perhaps by a factor 3–4 for higher-extinction regions.

In the near future, we intend to recalibrate the structural parameters for the TRILEGAL bulge model, which were last updated in Vanhollebeke et al. (2009). Improvements in the treatment of extinction are also expected: in particular, we suspect that TRILEGAL is currently weighting the extinction too heavily toward close distances along the line of sight in bulge regions. Improving the treatment of extinction is also a high priority for future work. PSF-fitting photometry for the VVVX survey, which does cover the full set of comparison fields chosen here,[19] would greatly aid this comparison, but this too is deferred to future developments.

4.3. Example 3: Eclipsing Binaries in the MW

Eclipsing binaries have been simulated with the SynthEc code, described in Appendix A. The left panel of Figure 15 presents their density across the sky for the case $f_{\rm bin} = 1$, that is, taking into account that we simulated only one-tenth of the expected binaries. For the same case, the right panel shows the histogram of eclipsing binaries maximum *r*-magnitude variations, $\Delta r_{\rm max}$. Histograms for the other filters are very similar. This histogram provides a rough upper limit to the number of eclipsing binary systems that LSST may detect. Indeed, these counts do not take into account the crowding limits (Section 4.6 below), and the binary fraction $f_{\rm bin}$ is surely lower than 1. Moreover, detection of eclipses with $\Delta r_{\rm max} \lesssim 0.01$ and in faint systems will be intrinsically difficult, and eclipse detections will depend on the eclipse duration and on the LSST timetable of observations. A precise estimate of the detectable eclipses is possible only after a detailed simulation of the LSST cadence and footprint, as done by Geller et al. (2021). Our upper limits appear in rough agreement with their estimates.

4.4. Example 4: Classical Cepheids in the MW

In our $f_{\rm bin} = 0$ simulations, classical Cepheids are single stars crossing the instability strip, most of them while on the core helium burning stage, and with maximum ages of a few hundred megayears. They are identified and attributed periods by means of the theoretical relations and tables provided in Bono et al. (2000), which describe the blue and red edges of the instability strip, and the logarithm of periods, as a function of $\log L$, $\log T_{\rm eff}$, $\log M$, and the metallicity Z, for both fundamental and first overtone modes. Importantly, the relations are inter/extrapolated as a function of $\log Z$, and applied only in the interval $2.5 < \log(L/L_\odot) < 4.8$.

Figure 16 shows the predicted distributions of periods for classical Cepheids in the MW, from the $f_{\rm bin} = 0$ simulation.[20] Total predicted numbers in the MW down to $i < 24$ mag are 7443 Cepheids, 6139 in the fundamental mode and 990 in the first overtone. These numbers certainly surpass those revealed by the most extensive catalogs to date—for instance the 1973 Galactic classic Cepheids classified by OGLE (Soszyński et al. 2020), the 2116 "all-sky" Cepheids (i.e., excluding the MCs) present in Gaia DR2 (Clementini et al. 2019), or the 3352 in the recent compilation by Pietrukowicz et al. (2021). Any detailed comparison with these numbers is made difficult by the uncertain detection efficiency of these surveys as a function of the mean magnitude and period. For instance, the bulk of Cepheids in the Gaia DR2 catalog is found at $G < 17$ mag; a

[18] We use the PSF photometry (table vvvPsfDophotZYJHKsSource) from VVV DR5, available at http://www-wfau.roe.ac.uk/vsa/.

[19] See, e.g., https://www.eso.org/sci/publications/announcements/sciann17186.html.

[20] The distribution for the MCs is of less interest, as present observations of MC Cepheids from OGLE (Soszyński et al. 2019) and Gaia DR2 (Clementini et al. 2019) are close to being complete.

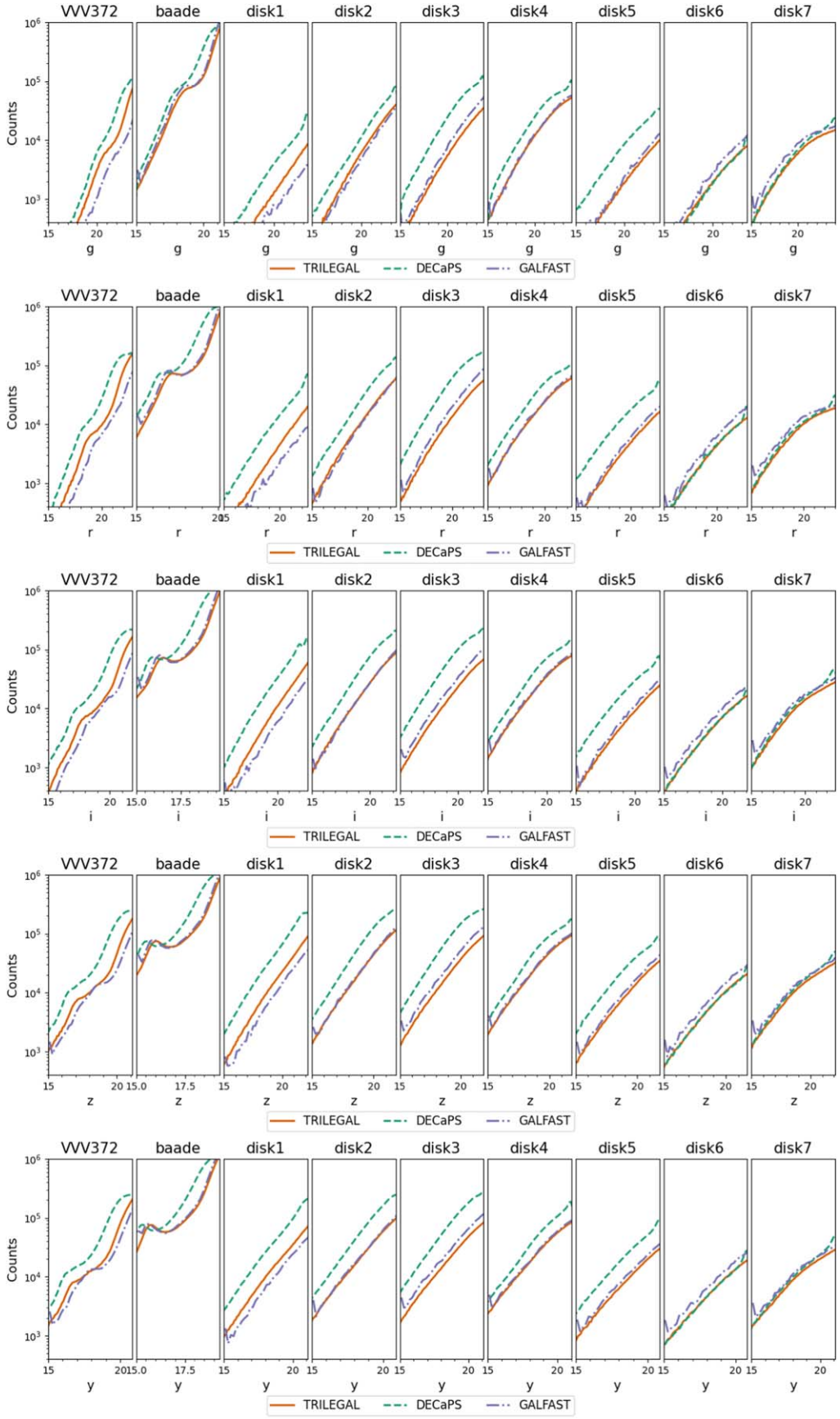

Figure 11. Comparison between the star counts in the present catalog (`TRILEGAL`; orange lines) with the previous `galfast` catalog (dashed–dotted blue lines), and the real star counts from DECaPS (dashed green lines), for the low-b areas depicted in Figure 9 and for all *grizy* filters (from top to bottom). All panels cover a similar range in magnitude with the exception of `VVV372` and `baade`, which are limited at the faint end where star counts start to decrease because of crowding. The number counts are computed in magnitude bins 0.1 mag wide. See Section 4.2.

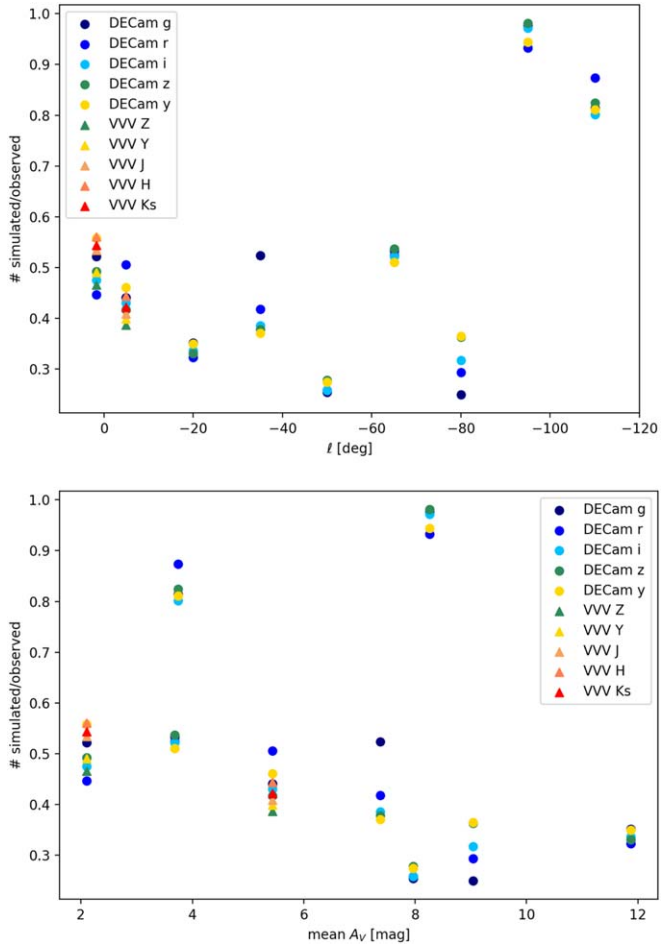

Figure 12. Ratio between star counts (in the sense $S =$ (simulated/observed) as a function of the Galactic longitude l (top panel) and mean extinction A_V (bottom panel). Circles show the ratio TRILEGAL/DECaPS while triangles show TRILEGAL/VVV. Filters are indicated in the legend. Note that the two clouds of points with (simulated/observed) $\gtrsim 0.8$ are identified with the outlier fields at longitude $|l| > 90°$. See Section 4.2.

similar cut in brightness reduces our simulated sample to 3457, or nearly half the total numbers for $i < 24$ mag. This still amounts to twice the numbers present in the Gaia DR2 catalog —which, however, is considered as very much incomplete due to the limited number of epochs included in DR2 for a significant fraction of the sky (see Section 5.2 in Clementini et al. 2019).

Even if the simulations seem to provide a correct order of magnitude for the total numbers of the Cepheids on the MW, it is worth reminding that these predictions are very dependent on uncertain prescription like the star formation rates and the metallicity distribution across the MW disk at young ages. Nonetheless, even if these total numbers might be over/underestimated, our simulations might still provide useful trends as a function of celestial coordinates and apparent magnitudes.

4.5. Example 5: Long-period Variables in the MW

Long-period variables (LPVs) are low- to intermediate-mass stars evolving along the red giant branch (RGB) and asymptotic giant branch (AGB), which undergo pulsation with periods of the order of a few days up to several hundred days, possibly displaying multiperiodicity. With its 10 yr baseline, LSST is expected to provide important data for the understanding of long-period variability, especially at the near-solar metallicities that characterize ample regions of the Galaxy. Such a knowledge might become crucial for the certification of LPVs as reliable distance indicators of galaxies farther than a few Mpc.

We simulate long-period variability only for TP-AGB (`label` $= 8$) stars and use the results from linear, radial, nonadiabatic pulsation models computed by Trabucchi et al. (2019). They provide best-fit relations overtone-mode periods expressed as power laws of the stellar mass and radius (their Equation (11)) as well as a best-fit expression for the fundamental mode period as a function of the mass, radius, and chemical composition (their Equation (12)). We adopt these formulae to compute the periods corresponding to radial pulsation in the fundamental mode (radial order $n = 0$) and in the first four overtone modes ($1 \leqslant n \leqslant 4$). These values are stored in the quantities `period0` to `period4` and their distributions are shown in Figure 17.

Which ones of these five pulsation modes are actually unstable in a given LPV, and thus potentially observable, depends on the structure of its envelope. The same is true for the most unstable (*dominant*) mode, whose signature is expected to be the strongest in the observed light curve of an LPV. These pieces of information are crucial for characterizing and interpreting observed variability data. Trabucchi et al. (2019) describe the stability of a given overtone mode in terms of a critical value of the stellar luminosity beyond which that mode tends to become stable. The critical luminosity can be computed as a function of the mass and chemical composition from their Equation (10), allowing us to establish which modes are stable and which ones are unstable for each simulated LPV. According to the scenario described by Trabucchi et al. (2019), the highest-order mode among the ones that are unstable is most likely dominant, and its radial order is stored in the quantity `pmode`.

Whether or not the dominant mode is actually observable depends on its amplitude, a quantity that cannot be predicted by models adopting the linear approximation of stellar pulsations, and that is therefore not included in the current simulation. The dominant mode should therefore be interpreted as the most likely to be observable. The same is true in the case of multiperiodic LPVs, having multiple modes that can be excited simultaneously. As a rule of thumb, modes neighboring the dominant (i.e., with radial order `pmode`± 1) are the most likely to be excited.

The inclusion of amplitude information is planned for a future version of the simulation, together with updated results for fundamental-mode pulsation from nonlinear calculations (see Trabucchi et al. 2021). We point out that some improvements can be independently implemented by the users. In particular we provide in Appendix B an example Python script to compute more accurate fundamental-mode periods for Miras and related LPVs pulsating in the fundamental mode.

It is worth noticing that simulated LPVs far outnumber the classical Cepheids: indeed, 444 038 LPVs are included in Figure 17. They represent a large fraction of the thermally pulsing AGB stars in the MW, with the exception of those strongly obscured by their own circumstellar dust shell or by interstellar extinction. We remark that AGB stars brighter than the tip of the RGB amount to similar numbers in the $\sim 1/3$ of the M31 galaxy sampled by the Panchromatic Hubble Andromeda Treasury survey (see Girardi et al. 2020; Goldman et al. 2022), and that Gaia DR2 already contains over 150,000 LPVs with amplitudes larger than 0.2 mag (Mowlavi et al. 2018), with just a minor fraction of them being in the Magellanic Couds (see, e.g.,

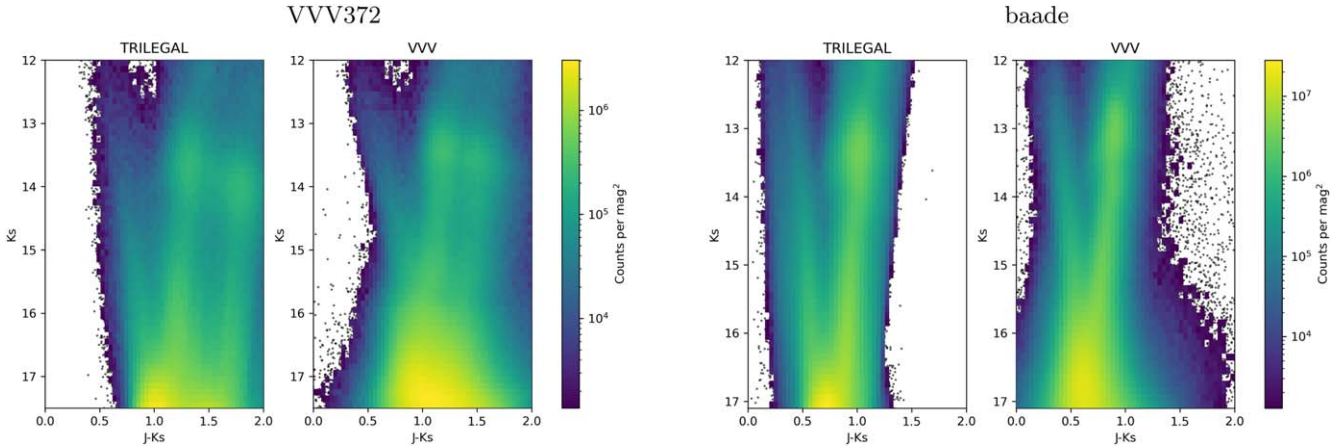

Figure 13. Comparison between TRILEGAL and VVV CMDs (or Hess diagrams), for the two areas in Figure 9 covered by the VVV survey. See Section 4.2. It is worth noting that the same main features appear in both the model and in the observed CMDs, although not exactly at the same colors and magnitudes. Much of these differences might be associated to the imperfect treatment of extinction in the models (see text).

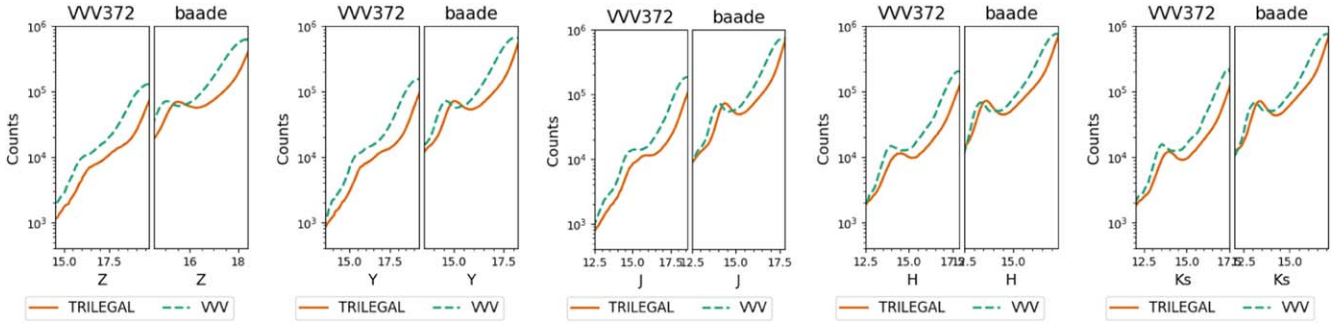

Figure 14. Comparison between the star counts in the present catalog (TRILEGAL, orange lines) with the real star counts from VVV (green lines), for the VVV372 and baade fields, and for all *ZYJHK*$_s$ filters. The range in magnitude is limited at the faint end at the point where star counts start to decrease because of crowding. The number counts are computed in magnitude bins 0.1 mag wide. See Section 4.2.

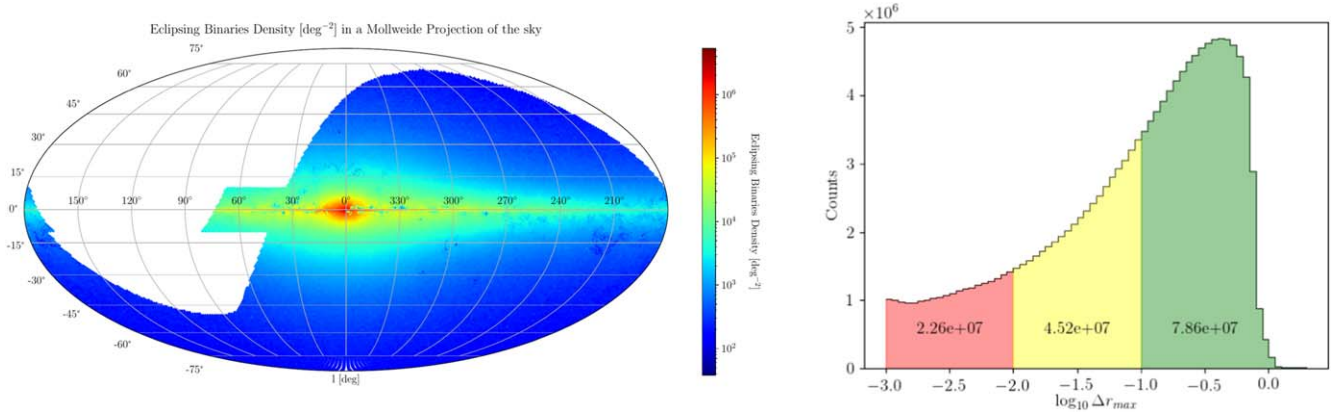

Figure 15. Left panel: counts of eclipsing binaries per square degree in the MW simulation for LSST with $f_{\rm bin} = 1$. Counts have been scaled up by taking into account that we simulated one-tenth of the expected binaries. Right panel: histogram of their maximum r-magnitude variations, $\Delta r_{\rm max}$. The red, yellow, and green areas divide eclipses into three groups separated at $\Delta r_{\rm max}$ of 0.01 and 0.1 mag. Total counts for each group are also indicated.

Lebzelter et al. 2018). Therefore, our predictions do not look exaggerated. However, without a detailed simulation of pulsation amplitudes and the cadence of the LSST observations, it is impossible to figure out the fraction that will be effectively identified as LPVs.

4.6. Application 1: Maps of Crowding Limit

The stellar density files are used in MAF to estimate the photometric errors due to stellar crowding, $\sigma_{\rm crowd}$, following the formalism developed by Olsen et al. (2003). A quantity that certainly matters for planning LSST observations is the "crowding limit", that is, the brightness below which the incompleteness caused by crowding becomes significant, assuming values above ∼50%. As demonstrated in a companion paper (W. I. Clarkson et al. 2022, in preparation), it closely corresponds to the point where we first reach $\sigma_{\rm crowd} = 0.25$ mag. It obviously depends on the instantaneous value of seeing and on the stellar luminosity function of the sky area being observed, in each passband (see Olsen et al. 2003).

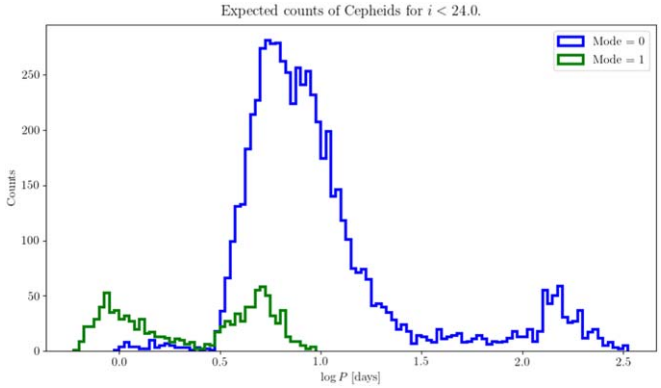

Figure 16. Histograms of classical Cepheids periods in the LSST MW simulation with $f_{\rm bin} = 0$. The two histograms are color coded according to the dominant mode: blue if fundamental mode, green if first overtone.

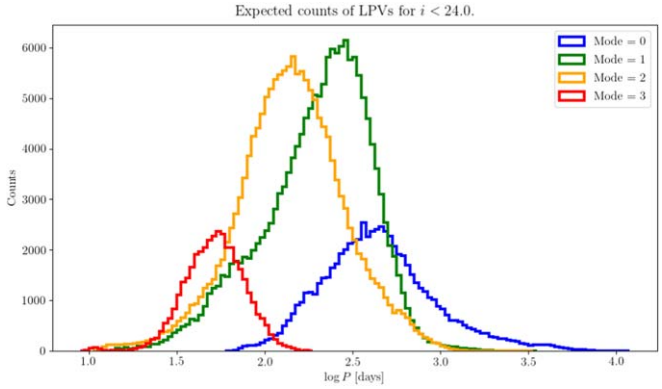

Figure 17. Histograms of LPVs periods in the LSST MW simulation with $f_{\rm bin} = 0$. The histograms are color coded according to the dominant mode, going from the fundamental to the third overtone.

Figure 18 shows crowding limits maps in the simulation with $f_{\rm bin} = 0$ and seeing 0.″6 for all LSST filters. This seeing is slightly better than the 0.″65 median value expected for the LSST main survey (LSST Science Collaboration et al. 2009). It can be noticed that severe crowding is expected only at limited areas across the bulge and central bodies of the Magellanic Clouds. In the case of *u*-band observations, crowded areas are limited to the central part of the LMC and to tiny spots in the bulge (including Baade's Window). Also, it can be noticed that the crowding limit is predicted to shift rapidly to brighter magnitudes as we move from the external to central areas of the bulge. At its off-plane boundaries, this rapid shift is a consequence of the bulge LF presenting a maximum (or, in some cases, an extended plateau) in a limited range in brightness corresponding to the red clump. A more gradual distribution of crowding limit is found closer to the plane, where the simulated LFs are significantly smoothed by the extinction along the line of sight.

Figure 19 presents additional maps for the *r* band and seeings of 0.″4 and 0.″7, hence illustrating how the crowding limit changes with this parameter. It becomes evident that a seeing as small as 0.″4 can make ample areas of the bulge to become "uncrowded"—that is, with high completeness, although possibly affected by significant photometric errors, up to 0.25 mag—especially at the photometric depth reached by the single visits.

4.7. Application 2: Maps of Star-to-galaxy Counts Ratio

Figure 20 shows the expected star-to-galaxy counts ratio in the *i* band, for both the single visit ($i < 24$ mag) and for the fiducial coadded depth ($i < 26.8$ mag). The star counts in this case come from the simulated LFs present on MAF, while the galaxy counts come from Equation (3.7) of LSST Science Collaboration et al. (2009):

$$N_{\rm gal} = 46 \times 10^{0.31(i_{\rm max}-25)} \text{galaxies arcmin}^{-2}. \quad (2)$$

We note that the latter is derived from observations in the $20.5 < i < 25.5$ interval (from Hoekstra et al. 2006; Gwyn 2008), and that our star counts start becoming incomplete for $i \gtrsim 26$ mag (given the cut at $r < 27.5$ mag in the simulation). Despite these limitations, this simple model indicates clearly that ample areas of the LSST sky will be dominated by galaxy counts, even for the single visits, with the obvious exceptions of the Galactic plane, bulge, and Magellanic Clouds.

5. Conclusions

The present simulations are a useful resource to plan LSST observations, either in its complete catalog form provided in the Astro Data Lab, or in its "stellar density and luminosity functions" form provided in MAF. In the first case, users can explore the stellar distributions in color–magnitude and color–color diagrams, histograms of periods and depth of binary eclipses, etc., and perform detailed comparisons with available surveys. In the second case, users can quickly obtain maps of stellar densities, crowding limits, star-to-galaxy ratios, etc. Also, comparisons with the results from `galfast` can provide a minimum uncertainty to the predictions of the several LSST survey plans.

Our plan is to provide a few revised versions of these LSST simulations over the next few years. They will be simply added to the Astro Data Lab, in successive data releases. Among the many updates being planned for the next release, we have:

1. adopting 3D extinction maps (A. Mazzi et al. 2022, in preparation);
2. adopting a spatially variable photometric depth, following our predictions for the crowding limit at the best possible seeing conditions;
3. improved star formation histories across the Magellanic Clouds (Mazzi et al. 2021; A. Mazzi et al. 2022, in preparation);
4. including a reasonable fraction of DB white dwarfs;
5. fully implementing the improved prescriptions for the modeling of the TP-AGB phase (Pastorelli et al. 2019, 2020), long-period variability (Trabucchi et al. 2021), and close binaries (Dal Tio et al. 2021);
6. including a reasonable fraction of rapidly rotating stars (Costa et al. 2019; Girardi et al. 2020);
7. updating prescriptions for the thick disk and halo (Pieres et al. 2020);
8. implementing a more realistic model for kinematics (as in Bond et al. 2010; Loebman et al. 2012).

We remark that all these changes are already feasible at the present stage, requiring just the integration of different pieces of code into our simulation software. They represent the advantage of having a code in active development, and with the constant feedback resulting from fitting the available data from present large-scale surveys of Local Group galaxies.

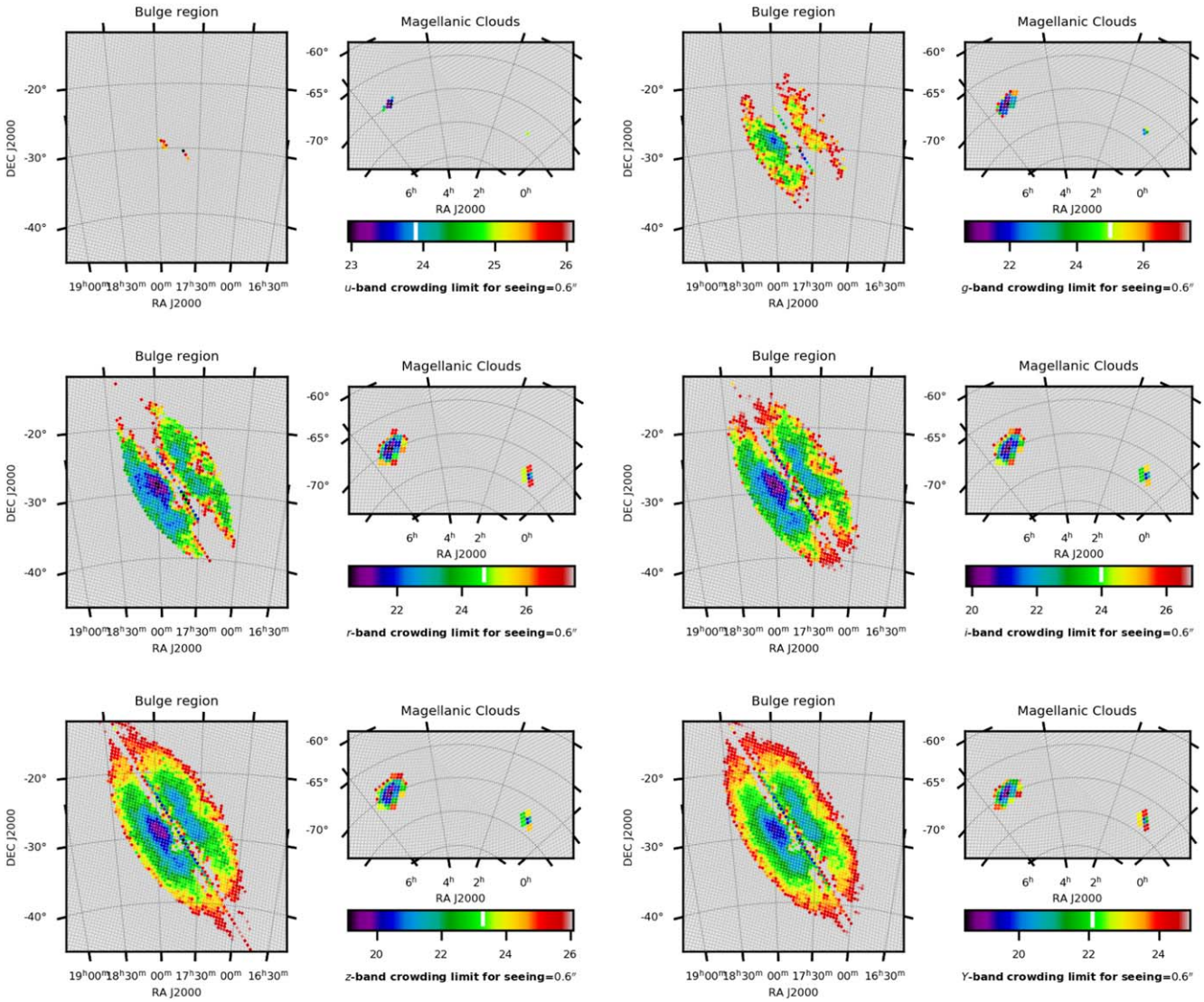

Figure 18. Maps of the crowding limit in the LSST simulation with $f_{\rm bin} = 0$, for the *ugrizy* bands (from the top-left to the bottom-right panels) and for a uniform seeing value of $0\farcs6$ at all wavelengths. They are derived from the $n_{\rm side} = 128$ density maps. The color scale covers a maximum range of 7 mag, starting from the coadd limiting depth (gray level). We plot only the areas around the bulge and the Magellanic Clouds, as the remaining sky areas turn out to be above the crowding limit (although they have nonnegligible photometric errors due to crowding). The white horizontal line in the color scale signals the single-visit depth for every filter.

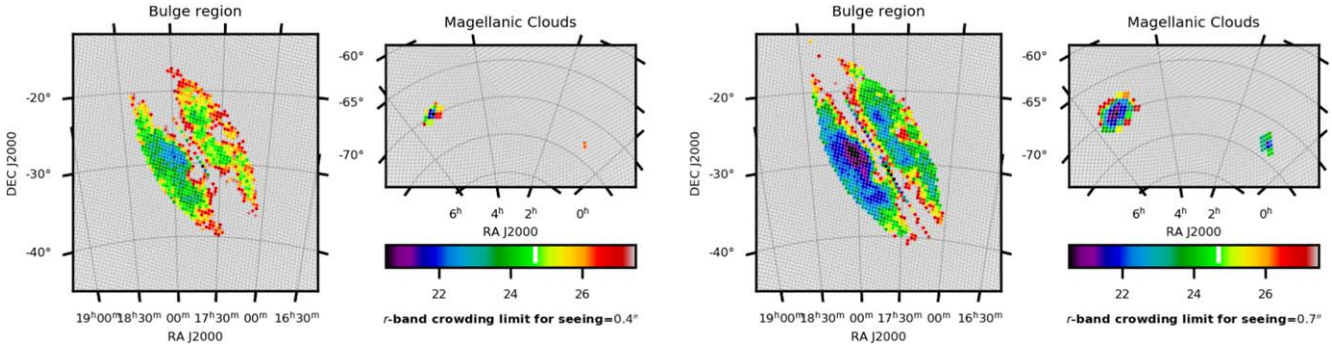

Figure 19. Same as Figure 18 but now presenting the crowding limit in the *r* band at two different values of seeing.

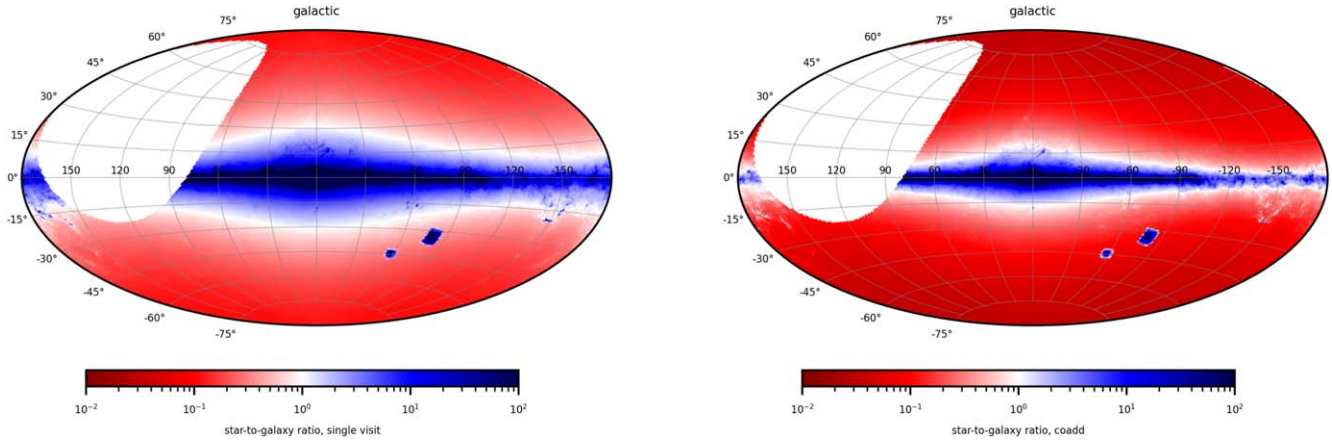

Figure 20. Star-to-galaxy ratio for a single visit ($i < 24$ mag, left panel) and for a coadd ($i < 26.8$ mag, right panel).

P.D.T., A.M., L.G., and P.M. acknowledge financial support from Padova University, Department of Physics and Astronomy Research Project 2021 (PRD 2021). Y.C. acknowledges NSFC No. 12003001. W.I.C. acknowledges support from the Preparing for Astrophysics with LSST Program, supported by the Heising-Simons Foundation and managed by Las Cumbres Observatory. M.J., Z.I., and P.Y. acknowledge the support from the DiRAC Institute, supported through generous gifts from the Charles and Lisa Simonyi Fund for Arts and Sciences and the Washington Research Foundation. A.B. acknowledges funding from PRIN MIUR 2017 prot. 20173ML3WW001/002. Many thanks to the Heising-Simons Foundation for the support, and to the entire SMWLV and TVS LSST Science Collaborations for the stimulating environment and feedback.

Facilities: Vera C. Rubin Observatory, NOIRLab Astro Data Lab (McManus & Olsen 2021).

Software: `TRILEGAL` (Girardi et al. 2005), `BinaPSE` (Dal Tio et al. 2021), `SynthEc` (this work), `YBC` (Chen et al. 2019), `HEALPix` (Górski et al. 2005), `MAF` (Jones et al. 2014), `matplotlib` (Hunter 2007).

Appendix A
The `SynthEc` Code for Eclipsing Binaries

`SynthEc` is a new C code developed by us to evaluate whether a binary system is an eclipsing binary. It is able to compute a synthetic light curve and to provide the maxima of magnitude variations. Moreover, it provides radial velocities amplitudes. The main hypothesis and features of the eclipsing binary model implemented in `SynthEc` are

1. the two stars of the binary system are assumed to be spherical (so the gravity darkening is neglected) and not interacting at the moment of the eclipse;
2. the velocity component that is orthogonal to the line of sight is assumed to be constant during the eclipse;
3. the fraction of the total flux of the obscured star observed during a transit or an occultation is computed by means of Equation (2) of Mandel & Agol (2002);
4. the limb darkening effect is taken into account by adopting the normalized specific intensity nonlinear law proposed by Claret (2000), but the reflection effect is neglected;
5. radial velocity amplitudes of the two stars can be computed as

$$K_{1,2} = \frac{2\pi a_{1,2} \sin i}{P\sqrt{1-e^2}}, \tag{A1}$$

where e is the eccentricity, a_1 and a_2 the semimajor axes of the two orbits in the center of mass frame, i is the inclination (randomly extracted from a uniform distribution in $\sin i$), and P is the orbital period.

We employ limb darkening coefficients computed in a homogeneous way with the `YBC` code (Chen et al. 2019), using the same LSST and Gaia filter transmission curves as in our main simulation.

Appendix B
Issues with the Data Lab Data Set

The present simulations were computed over a timescale of several months, during which some artifacts and possible improvements were identified in the simulation codes. Scripts at the Data Lab page will be provided to correct them, as far as possible.[21] They affect only a minor fraction of the simulated stars.

The first problem to be corrected is an excess of HB stars in old metal-poor populations, which turns our from a small mismatch between the ages of tracks on the RGB and on the zero-age horizontal branch, in the case of binary stars only. They can be identified (and removed) with a simple SQL command:

```
c1_Mass > 0.7 && c1_Mass < 0.9 && logAge > 10.0
&& c1_label == 4 && c1_logg > 3.2
```

The second correction results from a deep revision of the code used to model the fundamental-mode pulsation of LPVs (Section 4.5). Here we present a Python script for computing the fundamental-mode period based on results from nonlinear, radial pulsation models, using the analytic period–mass–radius relation of Trabucchi et al. (2021; their Equations (1) and (2)). These are incorporated into the function `nlP0MR(M, R)`, that takes the current mass `M` and radius `R` as arguments (possibly in the form of arrays). The script also include the definition of the function `Rdom0`(M) (based on Equation (4) of Trabucchi et al. 2021) to compute the critical radius beyond which the

[21] https://datalab.noirlab.edu/lsst_sim/

fundamental mode becomes dominant, given the current mass M of a star.

```
import numpy as np


# Base function
def _nlP0MR(M, R):
lM, lR = np.log10(M), np.log10(R)
l26 = np.log10(2.6)
logRb = np.log10(421.) + (0.952 if M < 2.6
else 0.114) *(lM - l26)
logPb = np.log10(440.) + (0.976 if M < 2.6
else -0.264) *(lM - l26)
logRs = np.log10(311.) + (1.590 if M < 1.0
else 0.654) *lM
logPs = np.log10(388.) + (1.808 if M < 1.0
else 0.502) *lM
alpha = np.log10(49.7) + (-0.279 if M < 2.6
else 0.544) *(lM - l26)
beta = (logPb - logPs)/(logRb - logRs)
if lR >= logRs:
return logPs
return logPb + (alpha if lR < logRb else beta)
*(lR - logRb)
# Turn into numpy ufunc for compatibility
with numpy arrays_
nlP0MR = np.frompyfunc(_nlP0MR, 2, 1)
# Non-linear Period-Mass-Radius relation,
takes current mass and radius
# (in solar units) as input, returns funda-
mental mode period in days
# M, R can be two numbers, two arrays, or a
number and an array
def nlP0MR(M, R):
return np.power(10., _nlP0MR(M, R).astype
(np.float64))


# Base function
def _Rdom0(M):
lM = np.log10(M)
return 2.130+1.150 *lM - 0.496 *np.power
(lM, 2)
# Turn into numpy ufunc for compatibility
with numpy arrays_
nlP0MR = np.frompyfunc(_Rdom0, 1, 1)
# Takes as input the current mass (in solar
units) and returns the
# critical radius beyond which the funda-
mental mode becomes dominant
# M can be either a number or an array
def Rdom0(M):
return np.power(10., _Rdom0(M).astype(np.
float64))


# Example
M = np.array([1., 2., 4.]) # Masses in solar
units
R = np.array([100., 150., 500.]) # Radii in
solar units
P0 = nlP0MR(M, R) # Compute period
print(P0)
Rd0 = Rdom0(M) # Compute critical radius
print(Rd0)
P0_is_dominant = (R > Rd0) # Check if funda-
mental mode is dominant
print(P0_is_dominant)
# the code above will return:
#     ≫>     [66.53463981     88.13808231
456.93000616]
#    ≫>    [134.89628826    269.92147725
439.11753351]
# ≫> [False False True]
```

Appendix C
Additional Comparisons with DECaPS Data

For the sake of completeness, Figure 21 presents a comparison between TRILEGAL and DECaPS CMDs (or Hess diagrams), for all areas drawn in Figure 9 that were not discussed in the main text.

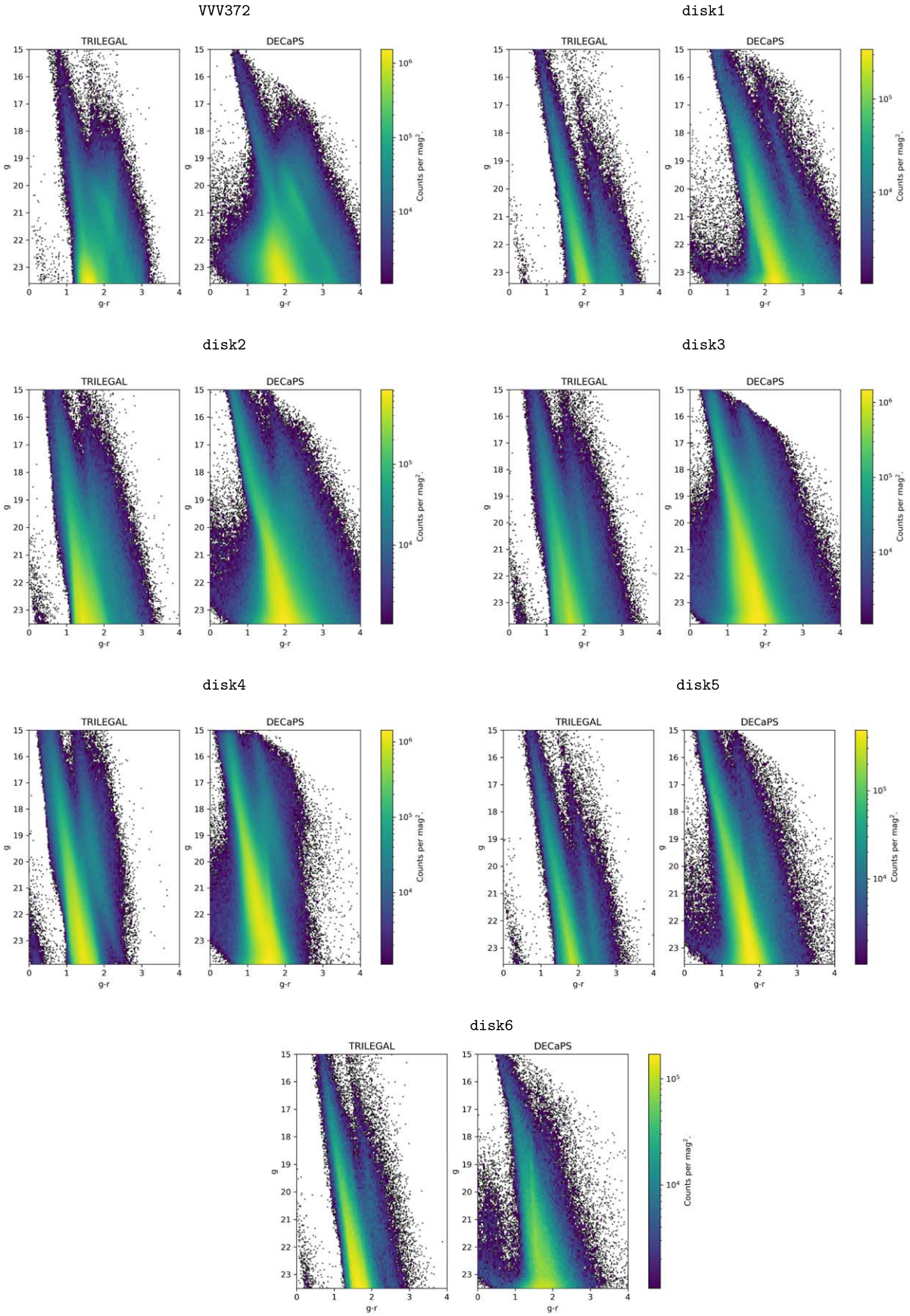

Figure 21. Comparison between TRILEGAL and DECaPS CMDs (or Hess diagrams), for areas drawn in Figure 9.

ORCID iDs

Piero Dal Tio https://orcid.org/0000-0002-0834-5092
Giada Pastorelli https://orcid.org/0000-0002-9300-7409
Alessandro Mazzi https://orcid.org/0000-0002-7503-5078
Michele Trabucchi https://orcid.org/0000-0002-1429-2388
Guglielmo Costa https://orcid.org/0000-0002-6213-6988
Alice Jacques https://orcid.org/0000-0001-9631-831X
Adriano Pieres https://orcid.org/0000-0001-9186-6042
Léo Girardi https://orcid.org/0000-0002-6301-3269
Yang Chen https://orcid.org/0000-0002-3759-1487
Knut A. G. Olsen https://orcid.org/0000-0002-7134-8296
Mario Juric https://orcid.org/0000-0003-1996-9252
Željko Ivezić https://orcid.org/0000-0001-5250-2633
Peter Yoachim https://orcid.org/0000-0003-2874-6464
William I. Clarkson https://orcid.org/0000-0002-2577-8885
Paola Marigo https://orcid.org/0000-0002-9137-0773
Thaise S. Rodrigues https://orcid.org/0000-0002-9414-339X
Simone Zaggia https://orcid.org/0000-0001-6081-379X
Mauro Barbieri https://orcid.org/0000-0001-8362-3462
Yazan Momany https://orcid.org/0000-0001-8946-8723
Alessandro Bressan https://orcid.org/0000-0002-7922-8440
Robert Nikutta https://orcid.org/0000-0002-7052-6900
Luiz Nicolaci da Costa https://orcid.org/0000-0002-7731-277X

References

Abbott, T. M. C., Adamów, M., Aguena, M., et al. 2021, ApJS, 255, 20
Bianchi, L., Efremova, B., Herald, J., et al. 2011, MNRAS, 411, 2770
Bianco, F. B., Ivezić, Z., Jones, R. L., et al. 2022, ApJS, 258, 1
Bond, N. A., Ivezić, A˘., Sesar, B., et al. 2010, ApJ, 716, 1
Bono, G., Castellani, V., & Marconi, M. 2000, ApJ, 529, 293
Bovy, J., Rix, H.-W., Green, G. M., Schlafly, E. F., & Finkbeiner, D. P. 2016, ApJ, 818, 130
Bressan, A., Marigo, P., Girardi, L., et al. 2012, MNRAS, 427, 127
Catchpole, R. M., Whitelock, P. A., Feast, M. W., et al. 2016, MNRAS, 455, 2216
Chabrier, G. 2001, ApJ, 554, 1274
Chen, Y., Girardi, L., Fu, X., et al. 2019, A&A, 632, A105
Chiba, M., & Beers, T. C. 2000, AJ, 119, 2843
Cioni, M. R. L., Clementini, G., Girardi, L., et al. 2011, A&A, 527, A116
Claret, A. 2000, A&A, 363, 1081
Clementini, G., Ripepi, V., Molinaro, R., et al. 2019, A&A, 622, A60
Costa, G., Girardi, L., Bressan, A., et al. 2019, A&A, 631, A128
Dal Tio, P., Mazzi, A., Girardi, L., et al. 2021, MNRAS, 506, 5681
Dehnen, W., & Binney, J. J. 1998, MNRAS, 298, 387
Dias, W. S., & Lépine, J. R. D. 2005, ApJ, 629, 825
Eggleton, P. 2006, Evolutionary Processes in Binary and Multiple Stars (Cambridge: Cambridge Univ. Press)
Geller, A. M., Polzin, A., Bowen, A., & Miller, A. A. 2021, ApJ, 919, 83
Girardi, L., Groenewegen, M. A. T., Hatziminaoglou, E., & da Costa, L. 2005, A&A, 436, 895
Girardi, L., Barbieri, M., Groenewegen, M. A. T., et al. 2012, Red Giants as Probes of the Structure and Evolution of the Milky Way (Berlin: Springer), 165
Girardi, L., Boyer, M. L., Johnson, L. C., et al. 2020, ApJ, 901, 19
Goldman, S. R., Boyer, M. L., Dalcanton, J., et al. 2022, ApJS, 259, 41
Górski, K. M., Hivon, E., Banday, A. J., et al. 2005, ApJ, 622, 759
Grady, J., Belokurov, V., & Evans, N. W. 2020, MNRAS, 492, 3128
Green, G. M., Schlafly, E., Zucker, C., Speagle, J. S., & Finkbeiner, D. 2019, ApJ, 887, 93
Gwyn, S. D. J. 2008, PASP, 120, 212
Harris, J., & Zaritsky, D. 2009, AJ, 138, 1243
Hoekstra, H., Mellier, Y., van Waerbeke, L., et al. 2006, ApJ, 647, 116
Holmberg, J., Nordström, B., & Andersen, J. 2009, A&A, 501, 941
Hunter, J. D. 2007, CSE, 9, 90
Hurley, J. R., Tout, C. A., & Pols, O. R. 2002, MNRAS, 329, 897
Ivezić, Ž., Sesar, B., & Jurić, M. 2008, ApJ, 684, 287
Ivezić, Ž., Kahn, S. M., Tyson, J. A., et al. 2019, ApJ, 873, 111
Jones, R. L., Yoachim, P., Chandrasekharan, S., et al. 2014, Proc. SPIE, 9149, 91490B
Jurić, M. 2018, galfast: Milky Way mock catalog generator, Astrophysics Source Code Library, ascl:1810.001
Jurić, M., Ivezić, Ž., Brooks, A., et al. 2008, ApJ, 673, 864
Kroupa, P. 2002, Sci, 295, 82
Lallement, R., Babusiaux, C., Vergely, J. L., et al. 2019, A&A, 625, A135
Lebzelter, T., Mowlavi, N., Marigo, P., et al. 2018, A&A, 616, L13
Lian, J., Zasowski, G., Hasselquist, S., et al. 2021, MNRAS, 500, 282
Loebman, S. R., Ivezić, Ž., Quinn, T. R., et al. 2012, ApJL, 758, L23
LSST Science Collaboration, Abell, P. A., Allison, J., et al. 2009, arXiv:0912.0201
Maíz Apellániz, J., & Weiler, M. 2018, A&A, 619, A180
Mandel, K., & Agol, E. 2002, ApJL, 580, L171
Marigo, P., Bressan, A., Nanni, A., Girardi, L., & Pumo, M. L. 2013, MNRAS, 434, 488
Marigo, P., Girardi, L., Bressan, A., et al. 2017, ApJ, 835, 77
Mazzi, A., Girardi, L., Zaggia, S., et al. 2021, MNRAS, 508, 245
McManus, S., & Olsen, K. 2021, Mirro, 2, 33
Miller Bertolami, M. M. 2016, A&A, 588, A25
Minniti, D., Lucas, P. W., Emerson, J. P., et al. 2010, NewA, 15, 433
Mowlavi, N., Lecoeur-Taïbi, I., Lebzelter, T., et al. 2018, A&A, 618, A58
Nataf, D. M., Gonzalez, O. A., Casagrande, L., et al. 2016, MNRAS, 456, 2692
O'Donnell, J. E. 1994, ApJ, 422, 158
Olsen, K., Bolton, A., Juneau, S., et al. 2019, BAAS, 51, 61
Olsen, K. A. G., Blum, R. D., & Rigaut, F. 2003, AJ, 126, 452
Pastorelli, G., Marigo, P., Girardi, L., et al. 2019, MNRAS, 485, 5666
Pastorelli, G., Marigo, P., Girardi, L., et al. 2020, MNRAS, 498, 3283
Pieres, A., Girardi, L., Balbinot, E., et al. 2020, MNRAS, 497, 1547
Pietrukowicz, P., Soszyński, I., & Udalski, A. 2021, AcA, 71, 205
Planck Collaboration, Abergel, A., Ade, P. A. R., et al. 2014, A&A, 571, A11
Portail, M., Gerhard, O., Wegg, C., & Ness, M. 2017a, MNRAS, 465, 1621
Portail, M., Wegg, C., Gerhard, O., & Ness, M. 2017b, MNRAS, 470, 1233
Rebassa-Mansergas, A., Agurto-Gangas, C., Schreiber, M. R., Gänsicke, B. T., & Koester, D. 2013, MNRAS, 433, 3398
Renedo, I., Althaus, L. G., Miller Bertolami, M. M., et al. 2010, ApJ, 717, 183
Robin, A. C., Reylé, C., Derrière, S., & Picaud, S. 2003, A&A, 409, 523
Rosenfield, P., Marigo, P., Girardi, L., et al. 2016, ApJ, 822, 73
Rossetto, B. M., Santiago, B. X., Girardi, L., et al. 2011, AJ, 141, 185
Rubele, S., Girardi, L., Kerber, L., et al. 2015, MNRAS, 449, 639
Saha, A., Vivas, A. K., Olszewski, E. W., et al. 2019, ApJ, 874, 30
Schlafly, E. F., Green, G. M., Lang, D., et al. 2018, ApJS, 234, 39
Soszyński, I., Udalski, A., Szymański, M. K., et al. 2019, AcA, 69, 87
Soszyński, I., Udalski, A., Szymański, M. K., et al. 2020, AcA, 70, 101
Trabucchi, M., Wood, P. R., Montalbán, J., et al. 2019, MNRAS, 482, 929
Trabucchi, M., Wood, P. R., Mowlavi, N., et al. 2021, MNRAS, 500, 1575
van der Marel, R. P., & Cioni, M.-R. L. 2001, AJ, 122, 1807
Vanhollebeke, E., Groenewegen, M. A. T., & Girardi, L. 2009, A&A, 498, 95
Wegg, C., Gerhard, O., & Portail, M. 2015, MNRAS, 450, 4050